Overshooting Convection, Cirrus, and the Cold Point Tropopause in Global Storm-Resolving Models and Satellite Observations

Jacqueline M. Nugent

A dissertation
submitted in partial fulfillment of the
requirements for the degree of

Doctor of Philosophy

University of Washington

2023

Committee:

Christopher S. Bretherton, Chair

Peter N. Blossey

Thomas P. Ackerman

Program Authorized to Offer Degree:
Atmospheric Sciences

University of Washington

Abstract

Overshooting Convection, Cirrus, and the Cold Point Tropopause in Global Storm-Resolving Models and Satellite Observations

Jacqueline M. Nugent

Chair of the Supervisory Committee:
Christopher S. Bretherton
Departments of Atmospheric Sciences and Applied Mathematics

Processes occurring in upper troposphere-lower stratosphere region (UTLS), especially overshooting convection and radiative heating from thin cirrus, play a key role in the Earth's climate system. The cold point tropopause, defined as the coldest temperature between the upper troposphere and lower stratosphere, is particularly important for determining the moisture content of the lower stratosphere, which feeds back onto the surface warming rate. This work aims to address how the cold point tropopause, overshooting convection, and cirrus are related using five 40-day simulations of global storm-resolving models in addition to 4 years of active and passive satellite observations.

We evaluate how convection that overshoots the cold point is distributed across the tropics and find that overshoots only somewhat favor warm land areas over warm ocean regions. The general geographic distribution in cold point overshoots is reproduced by the GSRMs. We also look at radiatively active cirrus near the cold point that are capable of producing a radiative heating rate strong enough to loft and cool the cold point. The GSRMs tend to simulate radiatively active cold point cirrus, as well as thin stratospheric cirrus, much less often than in the observations.

Still, despite the differences in the details of how the models simulate cold point overshoots and cirrus, we find consistent relationships between the cold point, overshooting

convection, and cirrus in the GSRMs over oceans. Areas with more frequent cold point overshoots were associated with cooler mean cold point temperatures and higher cold point heights. No significant relationship was found between the mean cold points and areas of more frequent radiatively active cold point cirrus, suggesting that this mechanism does not strongly influence the cold point temperature or height. Further work examining longer GSRM simulations is needed to better understand the role of cold point-overshooting convection and cirrus lofting in setting the cold point tropopause in the context of other UTLS processes.

TABLE OF CONTENTS

LIST OF FIGURES

LIST OF TABLES

GLOSSARY

AFR: 18° × 42° latitude-longitude region in Africa (7°W–35°E, 0°–18°N)

AMZ: 30° × 25° (Ch. 2; 47°W–72°W, 30°S–0°) or 10° × 10° (Ch. 4; 65°W–55°W, 30°S–20°S) latitude-longitude region in Amazonia

DYAMOND2: DYnamics of the Atmospheric general circulation Modeled On Non-hydrostatic Domains phase 2 (boreal winter)

ECP: 15° × 50° latitude-longitude region in the East-Central Pacific (150°W–100°W, 0°–15°N)

FWC: frozen water content

FWP: frozen water path

GEOS: Goddard Earth Observing System

GSAM: Global System for Atmospheric Modeling

GSRM: global storm-resolving model

ICON: Icosahedral Non-hydrostatic Model

IOE: 18° × 42° latitude-longitude region in the equatorial Indian Ocean (53°E–95°E, 12°S–6°N)

IOS: 15° × 50° latitude-longitude region in the southern Indian Ocean (50°E–100°E, 15°S–0°)

IWC: ice water content

IWP: ice water path

OLR: outgoing longwave radiation

SCREAM: Simple Cloud-Resolving E3SM Atmospheric Model

SCA: $10° \times 10°$ latitude-longitude region in South-Central Africa (20°E–30°E, 17°S–7°S)

X-SHIELD: eXperimental System for High-resolution prediction on Earth-to-Local Domains

SPC: $15° \times 50°$ (Ch. 2; 165°E–145°W, 20°S–5°S) or $10° \times 10°$ (Ch. 4; 170°–180°E, 15°S–5°S) latitude-longitude region in the South Pacific Convergence Zone

T_B: brightness temperature

T_{CP}: cold point temperature

TIM: $10° \times 10°$ latitude-longitude region in Timor Sea (120°E–130°E, 12°S–2°S)

TTL: Tropical Tropopause Layer

UTLS: Upper Troposphere-Lower Stratosphere

WPC: $15° \times 50°$ latitude-longitude region in the West Pacific (130°E–180°E, 0°–15°N)

Z_{CP}: cold point height

ACKNOWLEDGMENTS

I am sincerely grateful to my advisor, Chris Bretherton, for training me to become a scientist and for his patience, support, and encouragement throughout my time at the University of Washington. I want to thank Peter Blossey and Tom Ackerman for their mentorship and continuous suggestions for how to make this work better. I also want to thank the rest of my committee members, Dennis Hartmann and Alex Anderson-Frey, for their feedback on this work.

I also wish to thank my undergraduate mentors, Michael Biggerstaff and Fred Carr, for helping me to get involved with my first research project years ago. I would not be where I am today without their guidance and encouragement at the beginning of my education.

This material is based upon work supported by the National Science Foundation under Grant No. OISE-1743753. I am grateful for the greater Partnerships in International Research and Education (PIRE) Cirrus community for the knowledge and support offered by everyone. I would also like to thank the team members at the German Climate Computing Center (DKRZ), who provided data management for the DYAMOND projects and facilitated my analysis of the large volume of data involved in such a project.

I want to thank my family for their unyielding support and encouragement throughout my studies, even from over 2,000 miles away. I am grateful to my cohort and all my friends in and out of Seattle, especially Andrew Willoughby, Valerie and Cody Zike, Emma Dillon, Matt Swann, Sami Turbeville, Adam Sokol, Clayton and Kayla Shuster Sasaki, Ashish Phal, Lily Hahn, and the "Try Hards." You have all made my time in graduate school infinitely more enjoyable and I value your friendship and continuous support. I also want to thank Duschka Fowler-Dunning, True, and the rest of the Brackenhollow Stables family for giving

me a place to reset each week. Lastly, I want to thank my beloved cat, Clawsius-Catteyron, for the emotional support she has unknowingly provided over the years.

Chapter 1

INTRODUCTION

The upper troposphere-lower stratosphere region (UTLS) is a critical yet imperfectly understood aspect of the Earth's climate system. Processes occurring within the UTLS affect the temperature and moisture content of the lower stratosphere, which in turn can affect the surface warming rate (Brewer, 1949; Solomon et al., 2010). The temperature of the cold point, defined as the coldest level within the UTLS, is particularly important for determining the moisture entering the lower stratosphere (Holton & Gettelman, 2001; Dessler, 2002). Convection that overshoots the cold point can directly and indirectly influence this moisture content (e.g., Vernier et al., 2011; Corti et al., 2008; Ueyama et al., 2018; Dauhut & Hohenegger, 2022). Thin cirrus that are often observed near the cold point can also affect UTLS moisture (Jensen et al., 1996a) and can have a slight radiative heating effect strong enough to loft the cirrus layer (Jensen et al., 1996b; Fueglistaler et al., 2009). Both processes can also affect the temperature and height of the cold point tropopause (e.g., Hartmann et al., 2001; Durran et al., 2009; Suneeth et al., 2017), but it is unclear which mechanism plays a stronger role in setting the cold point temperature.

One of the difficulties in studying the UTLS is the lack of consistent observations at high resolutions in both space and time. Global storm-resolving models (GSRMs), high resolution cloud-resolving models with horizontal grid spacings below 5 km and explicitly resolved deep convection, have the potential to help fill this gap. These GSRMs have sufficient horizontal and vertical grid spacings to resolve individual overshoots and cirrus layers in the UTLS. The DYnamics of the Atmospheric general circulation Modeled On Non-hydrostatic Domains (DYAMOND) project was the first intercomparison of GSRMs that were initialized together but run freely for 40 days during boreal summer (Stevens et al., 2019). Analyses of phase 1 of

the DYAMOND project (DYAMOND1) have shown that the GSRMs can differ substantially in certain aspects of how they simulate deep convection and cirrus, but overall capture the general character of deep convection well (Nugent et al., 2022; Turbeville et al., 2022). GSRMs are rapidly evolving and improving as each new simulation is conducted. The second phase of the DYAMOND project (DYAMOND2) was recently completed and consisted of 12 GSRMs run together during boreal winter (Duras et al., 2021). GSRMs are promising tools to study the relationship between deep convection and the UTLS; however, because of the notable inter-model differences, GSRM studies must be grounded with observations.

In Chapter 2, I build a climatology of observed cold point-overshooting convection using a combination of active and passive satellite measurements. Using a proxy based on brightness temperature, I find that overshoots only somewhat favor land areas over warm ocean regions. This chapter has been submitted for publication as Nugent and Bretherton (2023).

In Chapter 3, I give a brief overview of the performance of the DYAMOND2 GSRMs in simulating deep convection to establish a baseline for later evaluation in Chapter 4. I compare the fidelity of a subset of five GSRMs in reproducing observed precipitation and outgoing longwave radiation.

Chapter 4 begins as a follow-up to Chapter 2, where I adapt the brightness temperature proxy to the DYAMOND2 GSRMs and evaluate the simulated distribution of cold point overshoots compared to the observed climatology. However, the main focus of this chapter is to use the GSRMs to study two mechanisms influencing the cold point tropopause, overshooting convection and radiative cirrus lofting, and see which seems to play a stronger role in determining the cold point temperature and height.

Chapter 2

TROPICAL CONVECTION OVERSHOOTS THE COLD POINT TROPOPAUSE NEARLY AS OFTEN OVER WARM OCEANS AS OVER LAND

2.1 Introduction

The tropical upper troposphere-lower stratosphere region (UTLS, ∼12–20 km) plays a critical role in the Earth's climate by influencing the composition of the lower stratosphere. The Brewer-Dobson circulation helps loft air from the upper troposphere into the lower stratosphere, which gets "freeze-dried" as it passes through the coldest temperatures near the tropopause, helping to set stratospheric moisture content (Brewer, 1949; Holton & Gettelman, 2001; Dessler, 2002). This mechanism is robust in observations; variations in stratospheric moisture are highly correlated with variations in the cold point temperature on subseasonal to interannual time scales (e.g., Randel & Jensen, 2013; Zhou et al., 2001b; Randel et al., 2004). This is significant for climate change. Many climate models project stratospheric water vapor will increase under 21st century greenhouse warming (Dessler et al., 2016; Tian et al., 2023), producing an additional greenhouse effect which would further increase the surface warming rate (Solomon et al., 2010).

However, this is a challenging modeling problem. In addition to nonlocal dynamical drivers, a complex, multiscale mixture of local physical processes is thought to regulate the cold point and overlying lower stratosphere. Though infrequent, convection that overshoots the cold point can alter the cold point temperature through entrainment (Gettelman et al., 2002; Kuang & Bretherton, 2004; Chae et al., 2011; Randel & Park, 2019) and modify stratospheric air through the turbulent mixing of ice and water vapor (e.g., Corti et al., 2008; Dion et al., 2019; Ueyama et al., 2023) and removal of vapor by deposition onto sedimenting ice

crystals (Jensen et al., 2007; Khaykin et al., 2022). Observations during the southeast Asian monsoon suggest ice injected by convective overshoots over land strongly affects the regional UTLS composition (Bucci et al., 2020). Cold point-overshooting convection may drive much of the transport between the upper troposphere and lower stratosphere (Pommereau, 2010; Vernier et al., 2011). It can also support the formation of thin UTLS cirrus through anvil detrainment or by generating gravity waves where ice can nucleate in the cold perturbations (Jensen et al., 1996b; Chang & L'Ecuyer, 2020; Jensen et al., 2016; Krämer et al., 2016).

Thin cirrus are common just below the cold point, especially around areas of frequent deep convection (Virts & Houze, 2015), with possible impacts on the UTLS from ice removal and radiative lofting (Jensen et al., 1996a, 1996b; Fueglistaler et al., 2009). An outstanding question is whether cold point-overshooting convection or thin cirrus has a greater impact on cold point temperatures and thus lower stratospheric moisture. Even global storm-resolving models, which explicitly simulate deep convection that reaches into the UTLS, have substantial intermodel spread in simulating the convection, cold point temperature, and cirrus that affect the UTLS (Nugent et al., 2022; Turbeville et al., 2022).

An important but imperfectly understood aspect of cold point-overshooting convection is its geographical and seasonal distribution, and how it differs between land and ocean regions. When defined using the 20 dBZ echo top height, the deepest tropical convection (Zipser et al., 2006) occurs mostly over land (e.g., Xian & Fu, 2015; Liu & Liu, 2016; Liu et al., 2020). But far too little large ice is typically lofted in cold-point overshoots to reach such reflectivities. Other observational studies using more sensitive radar thresholds (e.g., -20 to -30 dBZ) to identify high, cold convective cloud tops have found comparable frequencies of overshoots in convectively active land and ocean regions (Luo et al., 2008; Iwasaki et al., 2010; Takahashi & Luo, 2014; Li et al., 2022). Studies that used brightness temperature thresholds have even found more overshoots over oceans (Gettelman et al., 2002; Rossow & Pearl, 2007). The weaker land/ocean contrast in cold point overshoots vs. in intense mid-tropospheric updrafts is not fully understood. The upper-tropospheric thermal environment surrounding very deep oceanic convection may be more conducive for relatively weaker updrafts to reach

high altitudes (Kelley et al., 2010). Convective updraft velocity measurements in the UTLS are difficult and sparse, and extreme updraft strengths predicted by global storm-resolving models at 14 km altitude vary widely (Nugent et al., 2022).

A recent modeling study by Wu et al. (2023) found that in a warming climate, overshoots will increase much more over tropical oceans. Hong et al. (2005) and Aumann et al. (2018) also found warmer sea surface temperatures are correlated with more overshoots. Thus, documenting and understanding the spatial distribution of present-day cold point overshoots over ocean and land regions is important for predicting how overshooting convection may influence the UTLS in a changing climate.

Past studies using brightness temperature or -20 to -30 dBZ definitions of overshooting convection have been somewhat limited by relatively coarse data (Gettelman et al., 2002; Rossow & Pearl, 2007) or the twice-daily sun-synchronous sampling by the NASA A-Train (Luo et al., 2008; Takahashi & Luo, 2014; Li et al., 2022), which misses overshoots over land during the late afternoon diurnal cycle peak. Other studies used just one year of data (Iwasaki et al., 2010) or had only aggregate land-ocean statistics (Luo et al., 2008).

The goal of this paper is to achieve a climatology of the spatial distribution of cold point-overshooting convection across different land and ocean regions in a way that can later be generalized to model output. Via calibration with active sensor data, we show more convincingly than prior studies that a combination of passive satellite brightness temperatures and reanalysis with frequent global coverage is now sufficiently accurate to develop the desired climatology. In four years of data, we find evidence of occasional cold point-overshooting convection throughout the warmest, moistest parts of the tropics, with comparable frequencies over the Pacific warm pool and tropical land hot spots. Our proxy provides a useful observational benchmark for testing storm-resolving model simulations of tropical convective overshoot.

2.2 Data and Methods

2.2.1 Data Sets

We use ice water contents (IWC) from DARDAR-CLOUD v3.10 (Delanoë, 2023). The DARDAR product joins retrievals from the CloudSat cloud profiling radar and CALIPSO lidar on the NASA A-Train. The data have a horizontal footprint of 1.4 km and a vertical resolution of 60 m (Delanoë & Hogan, 2008, 2010; Cazenave et al., 2019). We use brightness temperatures from the NCEP/CPC L3 Half Hourly 4 km Global (60S–60N) Merged IR V1 (GPM_MERGIR) data set, which combines infrared brightness temperature data from several geostationary satellites (Janowiak et al., 2017). The GPM_MERGIR data set has a horizontal resolution of 4 km and a temporal resolution of 30 minutes.

Temperature profiles come from the ECMWF Reanalysis v5 (ERA5) model level data, which is available hourly on a $0.25° \times 0.25°$ grid with a vertical resolution of 300–400 m in the UTLS (Hersbach et al., 2017). The ERA5 reanalysis incorporates both Global Navigation Satellite System Radio Occultation (GNSS-RO) data and radiosonde measurements into the upper-level temperatures (Hersbach et al., 2020). We use reanalysis rather than the GNSS-RO or radiosonde data directly to have a collocated cold point temperature for each DARDAR retrieval. Overshooting convection occurs so infrequently that further restricting to near-coincident DARDAR and GNSS-RO data would insufficiently sample overshoots.

We consider two seasons: December-January-February (DJF) and June-July-August (JJA). Our DARDAR climatology is limited to 2007–2010, after which CloudSat only operated during the daytime. The ERA5 and GPM_MERGIR data are mapped onto the DARDAR track by selecting the data point closest in space and time to each DARDAR retrieval. However, the T_b values mapped onto the DARDAR data may not represent the true brightness temperatures at each pixel since the GPM_MERGIR and DARDAR data could be offset by up to 15 minutes.

2.2.2 Analysis Regions

We focus our analysis on four regions of approximately equal size for each season (shown in Figure 2.1a–d). These locations (three oceanic, one land) were selected to enclose areas of frequent active convection based on the climatological mean precipitation rate. For DJF, the regions are Amazonia (AMZ), the southern Indian Ocean (IOS), and the South Pacific Convergence Zone (SPC). For JJA, the analogous regions are Africa (AFR), the equatorial Indian Ocean (IOE), and the West Pacific (WPC). We also consider the East-Central Pacific (ECP) as a control, since this area rarely experiences deep convection as intense as that over the warmest oceans (e.g., Liu & Zipser, 2005; Liu et al., 2007), despite having similarly high time-mean precipitation rates. The coordinates of each region are listed in Table A.1. Across all regions, there are approximately 6.5M retrievals in DJF and 8.4M in JJA.

2.2.3 Cold Point Tropopause

We define the cold point as the level of the minimum temperature in the hourly 0.25° ERA5 temperature profiles. The 0.25° grid is small enough to capture fine spatial and temporal variations in the cold point but large enough to avoid interpreting the tops of individual convective clouds as cold point fluctuations. The 2007–2010 time-mean cold points (see Figure A.1) are higher (>17 km) and colder (around 191 K) in DJF than in JJA (altitude <17 km and temperature around 194 K), consistent with previous studies (e.g., Seidel et al., 2001; Kim & Son, 2012).

Compared to GNSS-RO and radiosonde data, the ERA5 climatological tropical cold point is generally <0.5 K warmer and ∼150 m lower (Tegtmeier et al., 2020a), although local variations in temperature or height may be larger. Hoffmann and Spang (2022) calculated an uncertainty of ±120–200 m in the lapse rate tropopause (LRT) height globally for ERA5 reanalysis. The ERA5 cold point, typically at or 0.5–1 km above the LRT (Munchak & Pan, 2014; Tseng & Fu, 2017; Pan et al., 2018), likely has a comparable uncertainty. In Section 2.3.3 we identify cold point overshoots by binning CloudSat-detectable radar echos

at intervals of 500 m relative to the local ERA5 cold point height. Echoes in the bin 500 m above the cold point presumably will usually lie above the true cold point despite these uncertainties.

2.3 Cloud Ice Above the Cold Point

2.3.1 Stratospheric Cirrus and Brightness Temperatures

To focus on cirrus associated with convective cold point overshoots, we bin DARDAR cloud ice by the difference between the brightness temperature (T_b) and the collocated cold point temperature (T_{cp}). This method is similar to that of Dauhut and Hohenegger (2022), who identified very deep convection in GSRM output by binning ice by the outgoing longwave radiation (OLR). Since brightness temperatures vary much more than cold point temperatures, large values of $T_b - T_{cp}$ correspond to high T_b and vice versa. We vertically bin the DARDAR data at cold-point-relative altitude levels. The ERA5 cold point height has a standard deviation of about 600 m within each analysis region, so using fixed altitude levels could incorrectly identify cold point overshoots. Following Pan and Munchak (2011), we instead use levels −500 m, 0 m, +500 m, and +1000 m relative to the local ERA5-estimated cold point height. We interpret "stratospheric" cirrus detected by DARDAR in the +500 m and +1000 m bins as very likely to be above the cold point height, despite uncertainties in measurement, reanalysis, and collocation.

Figure 2.1 shows the bin-mean IWC and bin counts at the cold point-relative levels in the four analysis regions shown in the top row. In all regions, cirrus is occasionally detected at least 500 m above the cold point across most of the $T_b - T_{cp}$ bins, corresponding to a broad range of brightness temperatures (bottom row). In fact, more stratospheric cirrus is collocated with high T_b than low T_b, which may seem counterintuitive. However, the coloring for overall count in each $T_b - T_{cp}$ bin (below the thick black line) indicates that there are many more bins with high than low brightness temperature. Thus, an atmospheric column with high T_b (i.e., relatively thin and/or low-lying cirrus) is much less likely to include cirrus

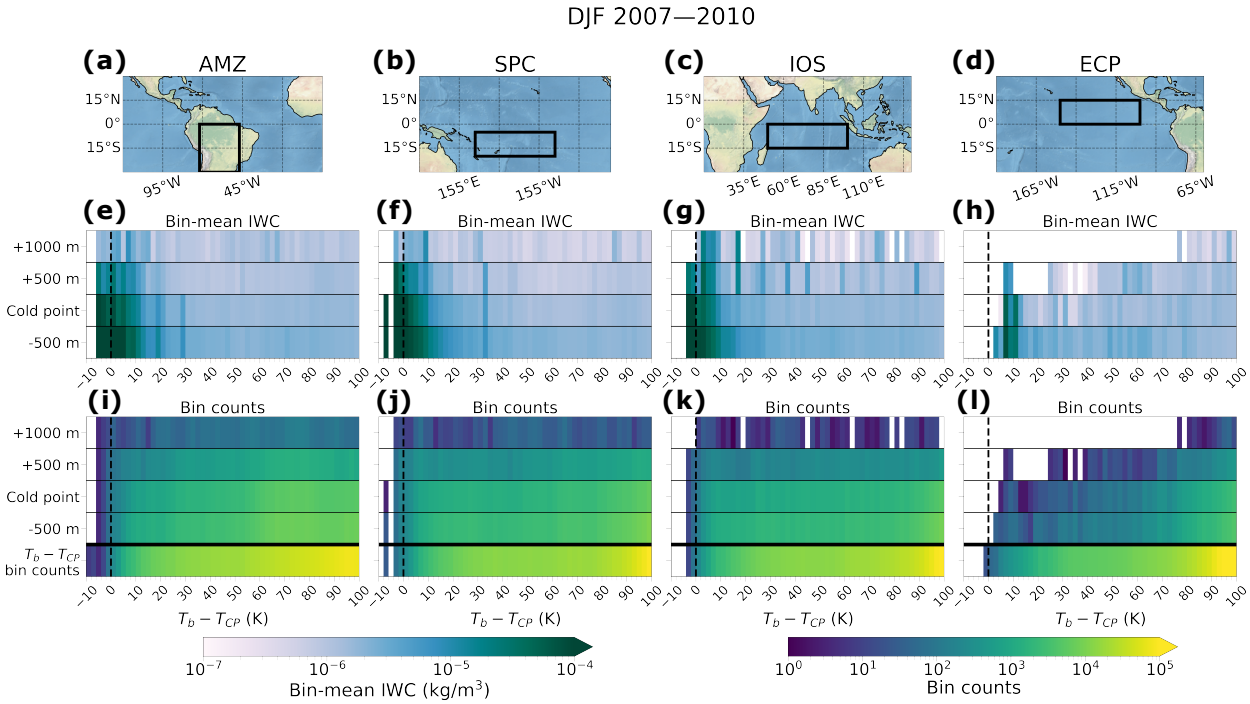

Figure 2.1: Cold point-relative cloud ice binned by $T_b - T_{cp}$ for all DARDAR pixels where ice is detected in DJF 2007–2010. (a)–(d) Maps of each analysis region; (e)–(h) bin-mean cloud-conditional IWC at 500 m below to 1000 m above the cold point height; and (i)–(l) bin counts conditioned on when DARDAR detects ice at each cold point-relative level. The row below the thick black line in (i)–(l) shows the total brightness temperature bin counts. The dashed lines in (e)–(l) mark where the brightness temperature equals the cold point. The bin width is 2 K.

above the cold point than one with low T_b.

When $T_b - T_{cp}$ is below ∼10 K, there is enhanced cloud ice (middle row; $\geq 5 \times 10^{-6}$ kg/m^3) at 500 m above the cold point in all regions except the ECP. At these low brightness temperatures, ice is almost always detected at 500 m above the cold point; i.e., the stratospheric cirrus bin counts are almost the same as the total bin counts. Together, these bin means and counts suggest that some of the DARDAR-detected stratospheric cirrus may indicate overshooting tops in both land and warm ocean regions.

There is some seasonal variability in the bin means and counts (see Figure A.2 for JJA), but the overall patterns between analogous regions in DJF and JJA are the same. One

difference is that bin counts at the +500 m level are lower in the WPC (Figure A.2f) than in the SPC (Figure 2.1f), meaning cirrus above the cold point is rarer in JJA over the Pacific warm pool. The ECP (Figure A.2h) has more ice above the cold point in JJA than in DJF (Figure 2.1h), but still has much less than in other regions.

2.3.2 Identifying Cold Point-Overshooting Tops

Most of the detections of ice above the cold point in Figures 2.1 and S2 are associated with thin cirrus clouds with high T_b. For the low $T_b - T_{cp}$ bins, the cirrus likely overlies deep convection. An actual overshooting top should not just have dense cloud ice but also larger ice particles lofted in the strong updraft that supports it; these particles should be detectable by the cloud radar. We therefore make binned plots restricted to include only radar-lidar pixels (Figure 2.2).

We anticipate that the dense cloud ice and low temperatures of overshooting tops should also cause particularly low brightness temperatures, possibly lower than the cold point temperature. The bottom row of Figure 2.2 shows that indeed, radar-detected ice above the cold point is almost exclusively associated with $T_b - T_{cp} < 10$ K, and at the coldest brightness temperatures, ice is almost always detected by the radar 500 m above the cold point. Thus we interpret radar-detected cirrus above the cold point as a cold point overshoot. We use the term "other stratospheric cirrus" for the remaining cirrus above the cold point that is detected only by lidar; some of this cirrus may be thin, while some of it may overlie extensive convective anvils or updrafts that do not overshoot the cold point.

Overshooting tops only comprise 1–2% of all tropical stratospheric cirrus, as inferred by comparing the fraction of DARDAR cold point overshoot pixels containing ice at the +500 m level detected by both radar and lidar (Figures 2.2 and S3) vs. lidar-only detections. The occurrence frequency of other stratospheric cirrus (0.9–2.5% in DJF, 0.4–1.5% in JJA) is approximately 50 to 100 times larger than the convective overshoot occurrence frequency (0.01–0.04% in both seasons). This relationship also holds for the ECP in JJA, but not in DJF when ice almost never occurs above the cold point there.

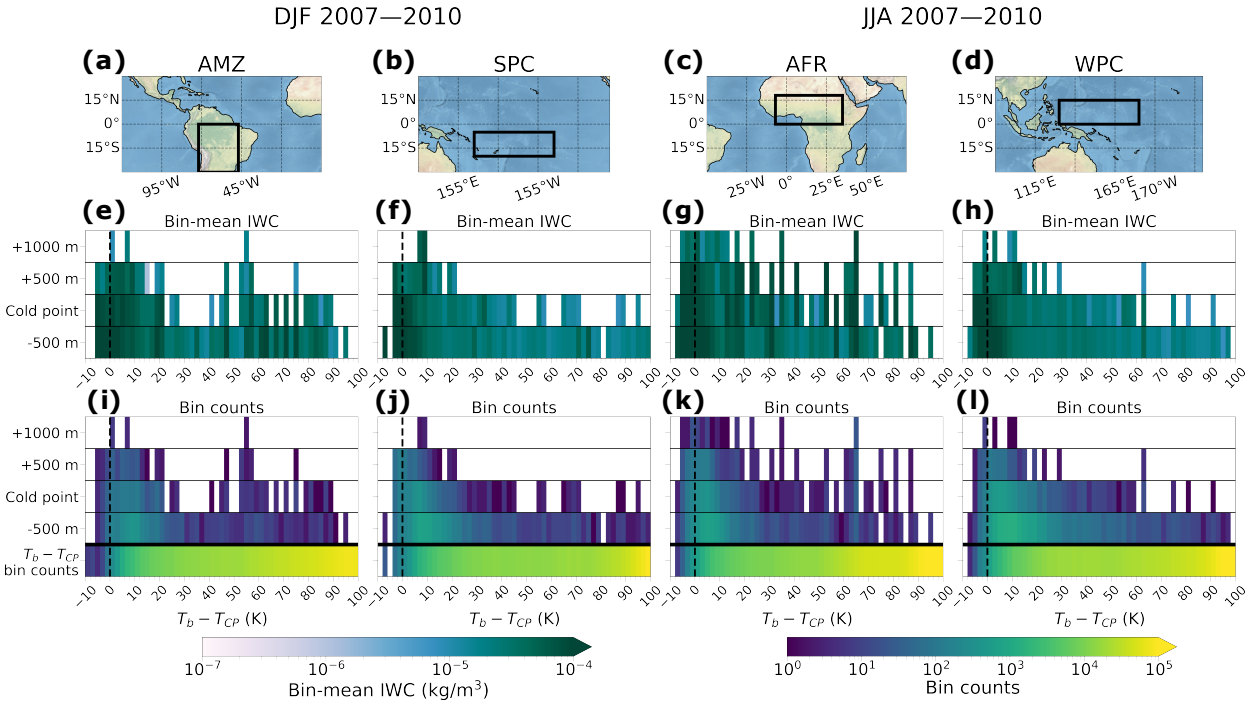

Figure 2.2: As in Figure 2.1 for select regions in DJF and JJA, but restricted to pixels in which the radar and lidar both detect ice.

2.3.3 Brightness Temperature Proxy for Overshoots

Using the DARDAR data, we can infer a relationship between brightness temperature and cold point overshoots. If the relationship is strong enough, T_b, which is much more broadly available than radar/lidar data, can be confidently used as an overshoot proxy. The reliability of this proxy will depend on the infrared opacity of the cloud extending above the cold point. We expect cold point overshoots to be ice-rich, but whether their T_b over the size of a GPM_MERGIR pixel is necessarily less than the cold point temperature is less obvious.

We calibrate the brightness temperature proxy by finding the fraction of DARDAR detections at a given value of $T_b - T_{cp}$ that are associated with radar-detected ice at 500 m above the cold point (top row in Figure 2.3). The probability of cold point overshoots steadily increases once $T_b - T_{cp}$ falls below 10 K. In AFR, AMZ, and SPC, there is about a 50% chance of radar-detected ice at 500 m above the cold point when $T_b = T_{cp}$ (solid lines in

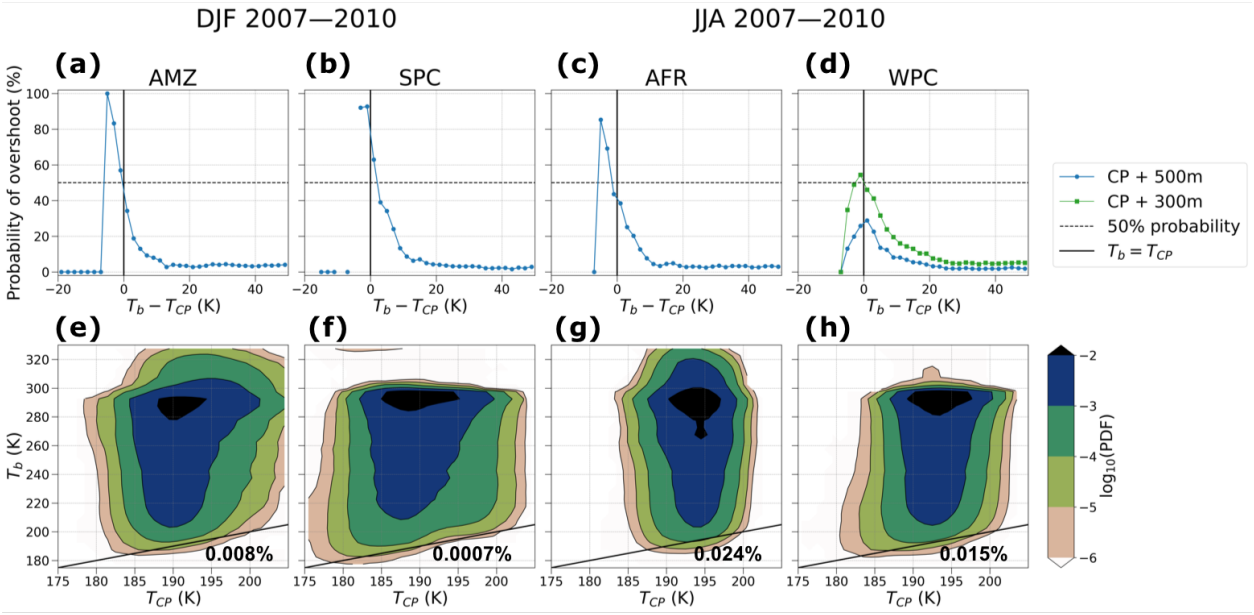

Figure 2.3: (a)–(d) Conditional probability of cold point overshoots (ice at 500 m above the cold point) as a function of $T_b - T_{cp}$. The dashed line indicates a 50% chance of cold point overshoots. (e)–(h) Joint brightness temperature-cold point histograms for all GPM_MERGIR data points. In all panels, the solid lines mark where the brightness temperature equals the cold point. The numbers on the bottom row of plots give the fraction of columns with $T_b < T_{cp}$. The same regions as in Figure 2.2 are shown.

Figure 2.3). The pattern is the same in the IOS and IOE (Figure A.4a, c). In the ECP, the probability of cold point overshoots never reaches 50%, and the brightness temperature is rarely less than the cold point (Figure A.4b, d). In the WPC, the probability of cold point overshoots of +500 m never exceeds 30%, but does exceed 50% at slightly lower overshoot heights (green line in Figure 2.3h). Unlike in other regions, the conditional probability of a convective overshoot over the WPC does not monotonically increase as $T_b - T_{cp}$ becomes more negative; more investigation is needed to understand what other factors may enable $T_b < T_{cp}$ with a low conditional probability of radar-detectable stratospheric cirrus in this region. Luo et al. (2008) argued that $T_b < T_{cp}$ is an unreliable indicator of cold point overshoots because overshoots with (without) radar-detected ice above the cold point may have brightness temperatures warmer (colder) than the cold point. While this may be true for

individual cases, our DARDAR results suggest that the $T_b < T_{cp}$ proxy is a statistically unbiased and physically plausible threshold for CloudSat-detectable convective overshoots.

The joint histograms of brightness and cold point temperatures in the bottom row of Figure 2.3 show the probability distributions for the entire GPM_MERGIR data set (i.e., not conditioned on DARDAR retrievals) in each study region/season. These probability distributions are similar to those from Gettelman et al. (2002) for the global tropics. Despite the differently-shaped distributions between land and ocean, the percentage of data points where $T_b < T_{cp}$ (below the solid lines) is similar: 0.008/0.007% in AMZ/SPC and 0.024/0.015% in AFR/WPC. In both Indian Ocean regions, 0.004% of data points have $T_b < T_{cp}$, and there are even less in the ECP (0.0002% in DJF, 0.002% in JJA). These patterns suggest there are slightly more cold point overshoots over hot spots of tropical convection over land than over the warmest oceans, and that convective overshoots are rare over convectively active but slightly less warm ocean regions such as the Pacific Intertropical Convergence Zone.

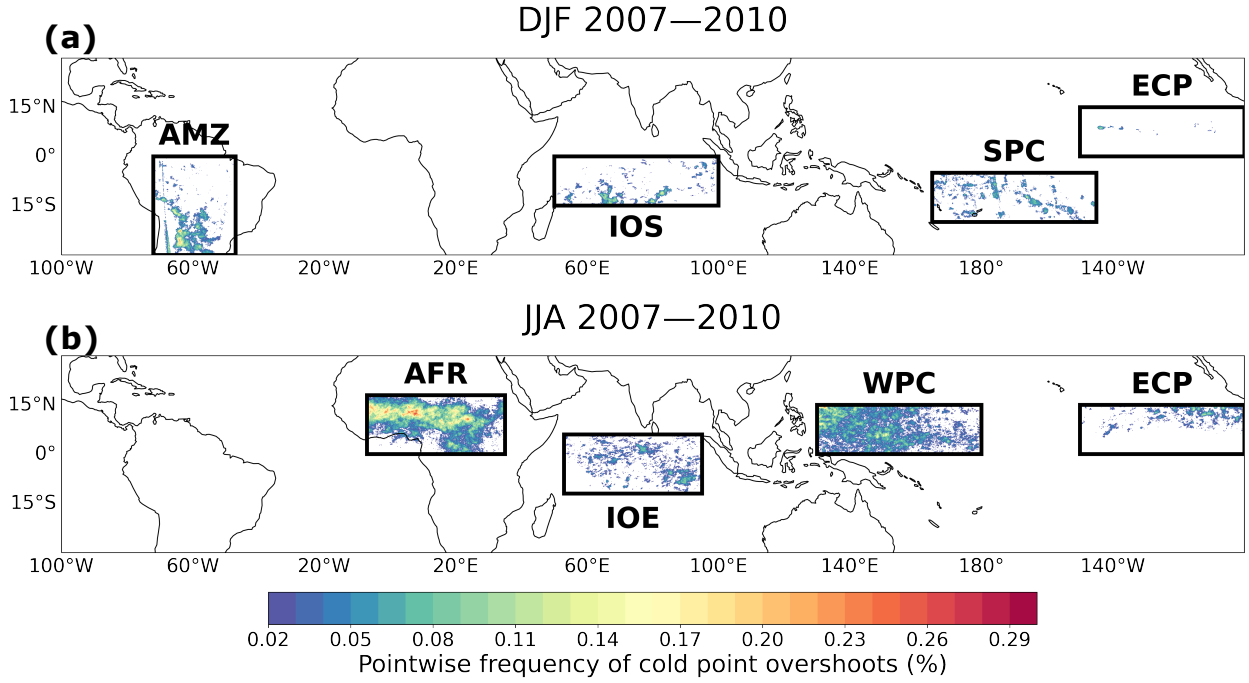

Figure 2.4: Frequency of cold point overshoots over time for (a) DJF and (b) JJA.

Finally, in Figure 2.4 we apply this proxy to estimate the spatial distribution of cold point overshoots within our study regions over the entire four-year GPM_MERGIR climatology, which past studies have not documented. With more data analysis, one could extend this analysis to look at the full global distribution and diurnal cycle of overshoots. Overshoots are 3–4 times more likely in JJA than DJF for analogous regions. Unsurprisingly, they are most common in AFR. Cold point overshoots are 30–40% more frequent over land regions (AFR, AMZ) than the warmest ocean regions (WPC, SPC). On average, the regional frequencies of cold point overshoots for DJF are 0.011% in the AMZ, 0.008% in the SPC, 0.006% in the IOS, and negligible (0.0004%) in the ECP. In JJA, they are 0.045% in AFR, 0.032% in the WPC, 0.016% in the IOE, and 0.014% in the ECP. These results corroborate past findings that cold point overshoots somewhat favor tropical land areas over oceans from Luo et al. (2008) and other studies that defined convective overshoot using a radar reflectivity threshold of -30 dBZ. Additionally, many of the areas of frequent cold point overshoots in the AMZ coincide with locations of the Andes Mountains, which suggests that orographic effects may be important for producing cold point overshoots.

2.4 Conclusions

We argue that $T_b < T_{cp}$ is a suitable proxy to identify cold point overshoots that uses only high-resolution (4 km) IR brightness temperature from a geostationary satellite and ERA5-inferred cold point temperature. At such low brightness temperatures, we find that there is a high probability of CloudSat radar-detectable cloud ice occurring above the cold point. Applying this proxy to 4 years of data over convectively active tropical land and ocean regions, we corroborate past findings that cold point-overshooting convection is only about 30–40% more common over land (AFR and AMZ) than Pacific warm pool regions (WPC and SPC). The cooler East Pacific region (ECP) has very few cold point overshoots, and the Indian Ocean regions (IOE and IOS) fall somewhere in between. Even in the regions where cold point overshoots are the most frequent, thin cirrus above the cold point cover ∼100 times more area than the cold point-overshooting tops. By using more data than available

to earlier investigators, we obtain seasonal maps of the overshoot frequency over our study regions that sample the full diurnal cycle and that could easily be extended to the global tropics.

In a follow up paper, we will adapt our $T_b < T_{cp}$ proxy to 40-day global storm-resolving model (GSRM) output from the DYAMOND intercomparison (Stevens et al., 2019) to compare cold point overshoots between models and observations. GSRMs explicitly simulate deep convection and have small enough (<5 km) horizontal grid spacing to capture convective overshoots. OLR, a routine model output, is converted to a broadband infrared brightness temperature similar, but not identical, to the satellite-derived brightness temperature inferred from emissions in a water vapor window wavelength. Understanding how well GSRMs can reproduce observed cold point overshoots in the current climate over both land and ocean will test the reliability of these models for simulating cold point overshoots and their influence on the UTLS in a warming climate.

Chapter 3

THE FIDELITY OF THE DYAMOND2 GSRMS IN SIMULATING DEEP CONVECTION

This chapter contains a brief overview of the performance of select GSRMs from the DYAMOND2 (boreal winter) intercomparison (Duras et al., 2021) in simulating deep convection and the climatological cold point. We evaluate the five GSRMs used in Chapter 4 (ICON, gSAM, GEOS, SCREAM, and X-SHiELD; see Table 4.1) by comparing the simulated precipitation and outgoing longwave radiation (OLR) between the models and observations. The DYAMOND2 models were run from January 20 to March 1, 2020, including a 10-day spinup period which we exclude from our analysis. In this chapter, we look at both the subset of the global tropics that is convectively active during boreal winter (30°S–10°N) as well as four representative 10° × 10° regions described in Chapter 4.2.2. This includes two land regions, Amazonia (AMZ) and South-Central Africa (SCA), as well as two ocean regions, the South Pacific Convergence Zone (SPC) and the Timor Sea (TIM). The cold point tropopause, overshooting convection, and cirrus near the cold point are evaluated thoroughly in Chapter 4.

3.1 Precipitation

We compare the DYAMOND2 GSRMs to a precipitation climatology using 10 years of GPM IMERG Final Precipitation L3 Half Hourly 0.1 degree x 0.1 degree V06 data (IMERG; Huffman et al., 2019) for the DYAMOND2 period during 2011–2020. Figure 3.1 shows the mean precipitation in the 10° × 10° accumulated over days 11–40 of the model run (30 January to 1 March 2020), excluding the spinup period. The IMERG climatology was first averaged over each year before accumulating the area-mean precipitation in the 30-day

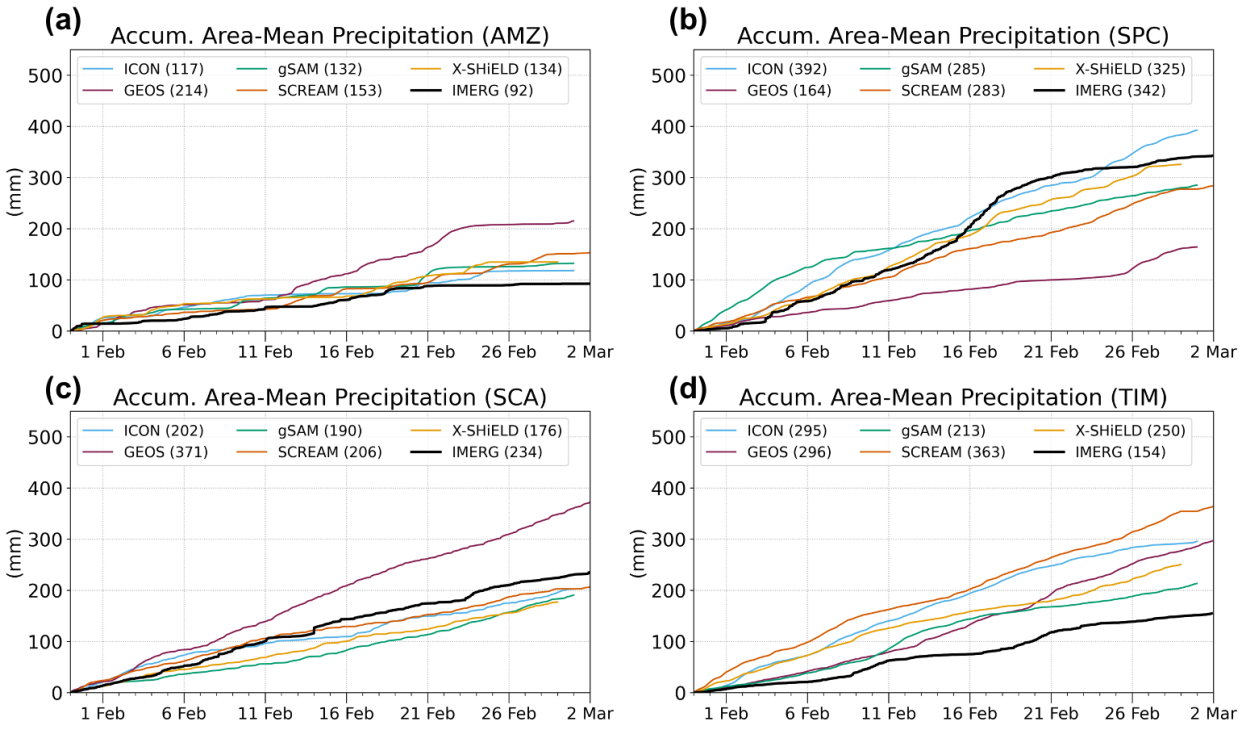

Figure 3.1: Accumulated 10° × 10° area-mean precipitation for the DYAMOND2 GSRMs and IMERG climatology for (a) AMZ, (b) SPC, (c) SCA, and (d) TIM. The numbers in the legend give the total accumulated area-mean precipitation (mm) for the 30-day period.

period. There is a much larger spread in the GSRM accumulated precipitation over oceans (Figure 3.1 b, d) than over land (Figure 3.1 a, c), consistent with the DYAMOND1 models during boreal summer (Nugent et al., 2022). GEOS has the most precipitation over land regions, but the least in the SPC. It falls in the middle of the models in TIM, likely because of enhanced precipitation over the islands in that region that are not present in the SPC. The other GSRMs overestimate the precipitation in TIM as well. However, in all other regions, the GSRMs (except for GEOS) do not significantly over- or underestimate the accumulated precipitation.

We also evaluate the diurnal cycle of precipitation in the analysis regions. The diurnal cycle of precipitation over land is a particularly important benchmark for GSRMs. With

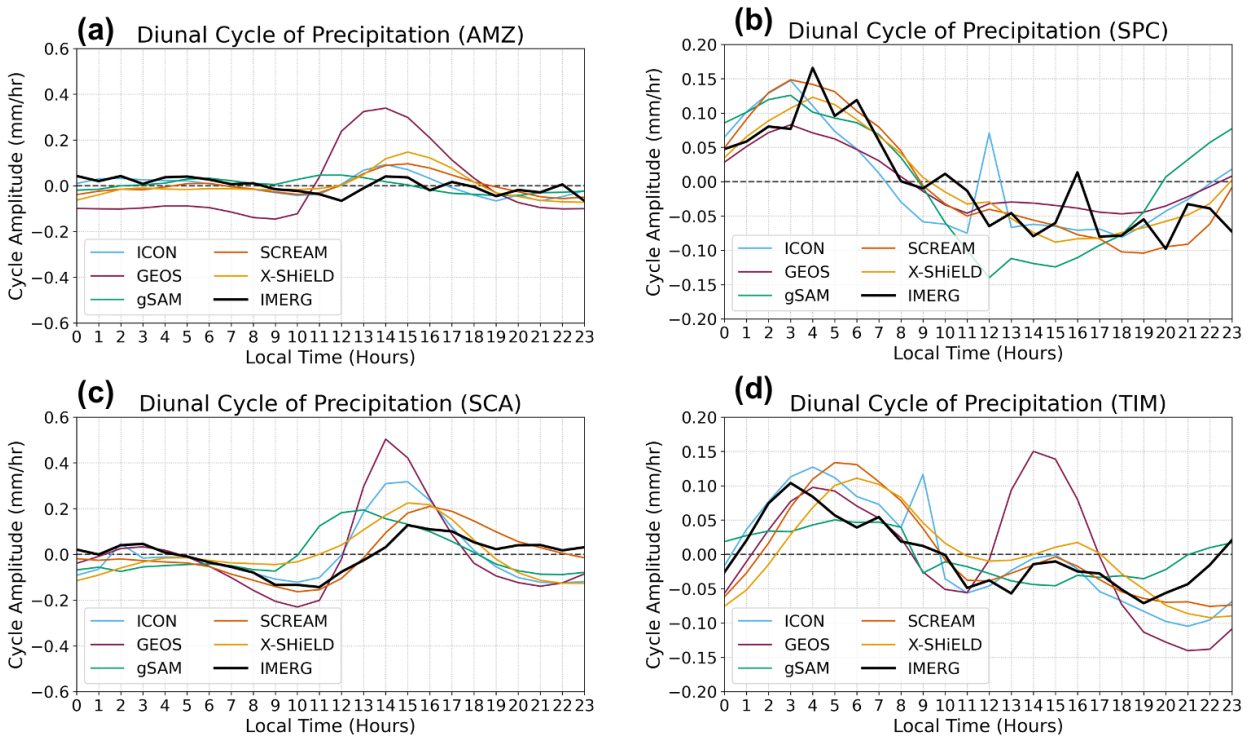

Figure 3.2: Diurnal cycle of precipitation (cycle amplitude) for the DYAMOND2 GSRMs and IMERG climatology for (a) AMZ, (b) SPC, (c) SCA, and (d) TIM.

explicitly resolved deep convection, GSRMs have the potential to correct a bias in global climate models with parameterized deep convection where the cycle tends to peak too early in the day (e.g., Bechtold et al., 2004; Duda & Gallus, 2013; Nugent et al., 2022). In Figure 3.2, we plot the diurnal cycle of precipitation over the land (left) and ocean (right) regions.

Over land (Figure 3.2 a, c), X-SHiELD, SCREAM, and ICON are closest to the observed peak in deep convection around 15:00–16:00 local time. GEOS peaks slightly too early, and gSAM peaks several hours too early. The cycle amplitude is generally overestimated, especially in the AMZ region, indicating that there is slightly too much precipitation over land in the GSRMs. In GEOS, however, the precipitation over land is substantially higher than in the observations. In the ocean regions (Figure 3.2 b, d) there is very good agreement in the timing and amplitude of the diurnal cycle between GSRMs and observations. Especially

in the SPC, the simulated cycles are very close to the observed cycle. The islands in the TIM region cause a secondary peak in precipitation in the afternoon in addition to the primary early morning peak. The GSRMs all capture this secondary peak, but in GEOS it is even more prominent than the early morning peak. The enhanced precipitation over land in GEOS likely causes the island signature to exceed the ocean signature in the diurnal cycle. Precipitation over land is therefore much too enhanced in GEOS, consistent with the overestimation in accumulated precipitation for the land regions. Overall, the GSRMs do a good job representing the land vs. ocean differences in the timing of the diurnal cycle.

3.2 Outgoing Longwave Radiation

Areas of extremely deep convection contain optically thick clouds that extend high into the troposphere, resulting in very low values of outgoing longwave radiation (OLR). Following Dauhut and Hohenegger (2022), we plot the first percentile over time of OLR in Figures 3.3–3.4 as a way to evaluate how the GSRMs simulate this extreme deep convection. We use CERES SYN1deg observations (Doelling et al., 2016) to evaluate the fidelity of the GSRMs. This data set is available hourly and on a $1^\circ \times 1^\circ$ grid, so we coarsen the GSRMs in both space and time to match the observations in Figure 3.3. In Figure 3.4, however, we keep the GSRMs at their native (15 minute, <5 km) resolution to evaluate the small-scale details in deep convection and do not include CERES.

Figure 3.3 shows the first percentile of coarsened (hourly, $1^\circ \times 1^\circ$) OLR in CERES and the GSRMs. There is no consistent pattern in how well the GSRMs do or do not reproduce the observed first percentile, meaning all of the models simulate deep convection in terms of OLR differently, particularly over land. GEOS and X-SHiELD look most like the observations over land, while the first percentile values in OLR over land are too high in the other models. Over the oceans, the models are somewhat more consistent with the observations, but the inter-model differences are still large. ICON and SCREAM (Figure 3.3 b, e) simulate OLR values that are too high everywhere, meaning it likely underestimates the intensity of the most extreme deep convection. gSAM (Figure 3.3 d) similarly underestimates deep convection

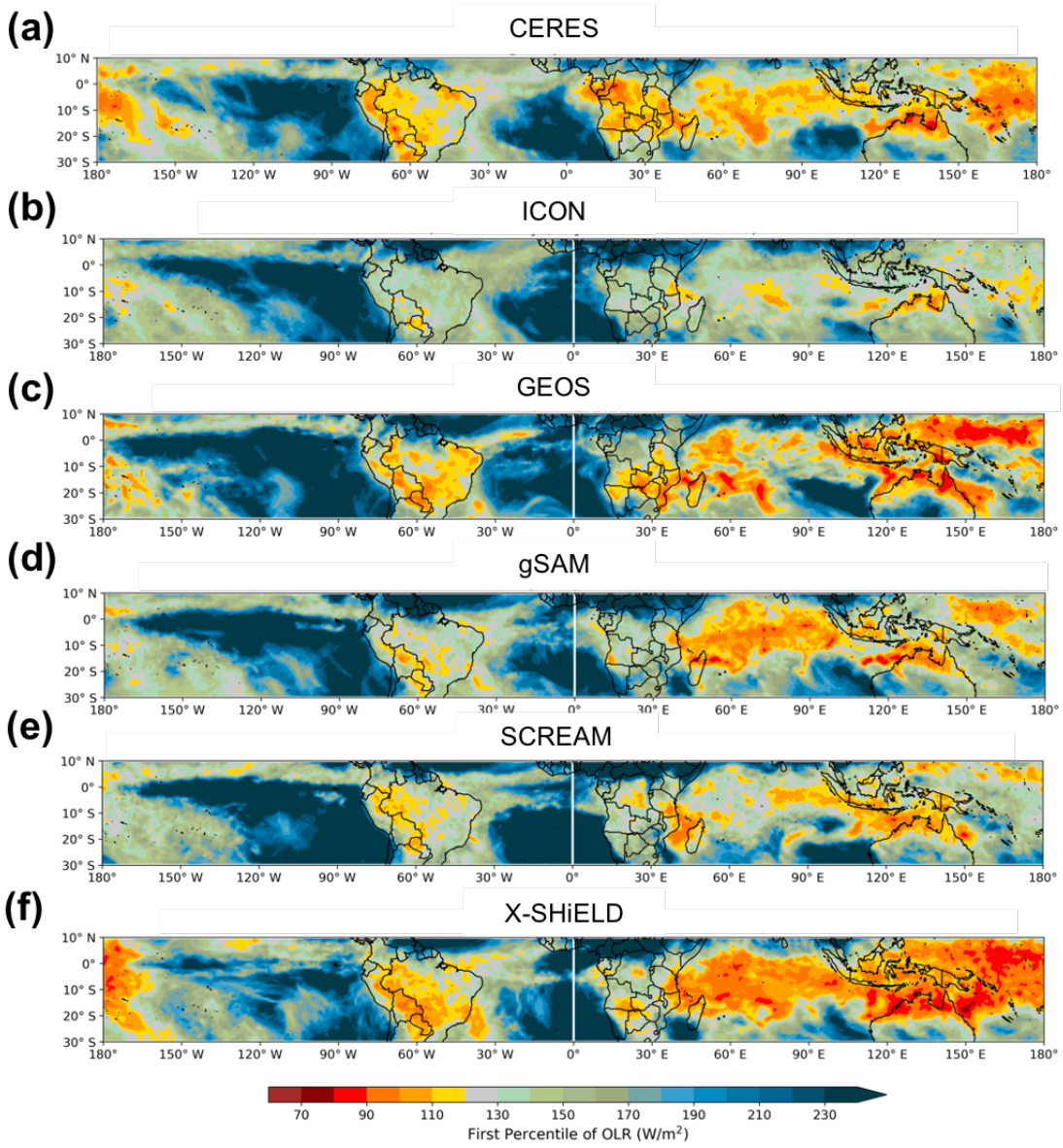

Figure 3.3: First percentile of coarsened (hourly, $1^\circ \times 1^\circ$) OLR over time at each grid point for (a) CERES SYN1deg, (b) ICON, (c), GEOS, (d) gSAM, (e) SCREAM, and (f) X-SHiELD. The vertical line near 0° longitude is an artifact of the coarsening and not part of the GSRM output. This figure is styled after Figure 3 in Dauhut and Hohenegger (2022).

over land with OLR values that are too high, but is reasonably similar to the observations over the ocean. X-SHiELD (Figure 3.3 f) simulates OLR values that are slightly too low everywhere, but especially over oceans, suggesting that it overestimates the intensity of deep convection over oceans. Surprisingly, GEOS (Figure 3.3 c) does not show significantly enhanced deep convection over land in the coarsened first percentile and in fact is the closest to the observations of all the GSRMs.

Figure 3.4 again shows the first percentile of OLR for the GSRMs, but for that native grid (15 minutes, 2.5–4 km). The $1^\circ \times 1^\circ$ and hourly averaging in Figure 3.3 smooths out many details in the models that are important for evaluating their simulation of extreme deep convection. In all GSRMs, the lowest values in OLR generally take up a much smaller area than $1^\circ \times 1^\circ$, so the first percentiles are consistently lower at the native grid scale than in the coarsened output. The overall spatial patterns in OLR are also much more consistent between models at the native scale, especially over land.

Most notably, ICON (Figure 3.4 a) and SCREAM (Figure 3.4 d) now look much more similar to the other GSRMs, although they still tend to have slightly higher OLR values. This change is likely due to the "popcorn"-like texture of convection seen in ICON and SCREAM (Nugent et al., 2022; Caldwell et al., 2021, respectively) where most of the convection is contained in small cells that get smeared away in the spatial averages rather than in more organized mesoscale convective systems. Similarly, the increased consistency in first percentile values over land at the native scale suggests that the convective organization over land is quite different between models. GEOS (Figure 3.4 b) has the lowest OLR values over land at the native scale. This pattern is consistent with its enhanced precipitation over land (Figures 3.1 and 3.2), which further indicates that deep convection over land in GEOS is too intense. However, since the land enhancement is not present in the coarsened OLR (Figure 3.3 c), the enhanced precipitation likely comes primarily from small-scale convective cells rather than larger convective systems. Regardless of these inter-model differences, the overall similarities in the spatial patterns of the first percentile of OLR suggests that the GSRMs simulate extreme deep convection reasonably well.

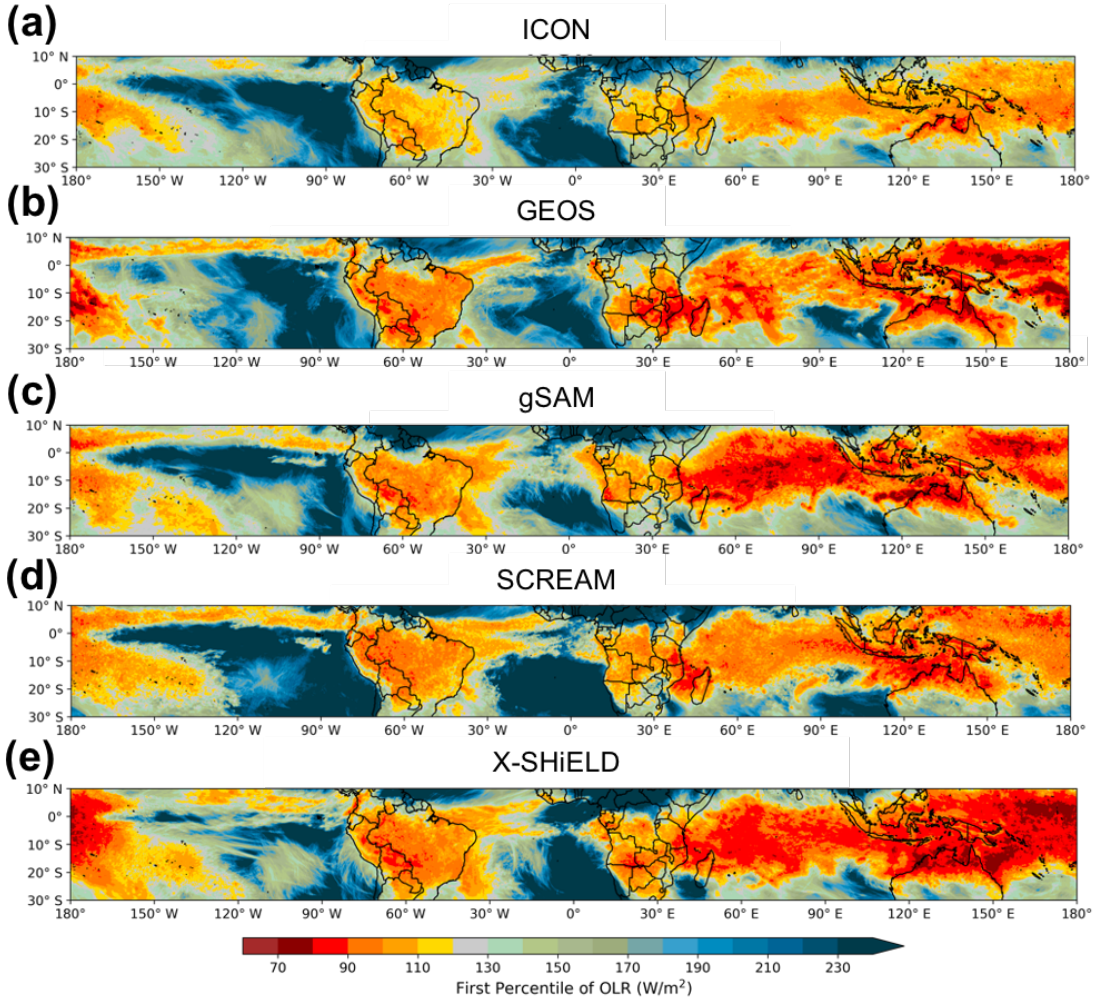

Figure 3.4: As in Figure 3.3, but for the native (15 min, <5 km) OLR in the GSRMs: (a) ICON, (b), GEOS, (c) gSAM, (d) SCREAM, and (e) X-SHiELD.

Chapter 4

WHAT SETS THE TROPICAL COLD POINT IN GSRMS? OVERSHOOTING CONVECTION VS. CIRRUS LOFTING

4.1 Introduction

Water vapor in the lower stratosphere can significantly impact the Earth's climate. Changes in the stratospheric moisture content can increase or decrease the surface warming rate (Solomon et al., 2010) The concentration of water vapor in the stratosphere is determined by processes in the upper troposphere-lower stratosphere (UTLS, ∼12—20 km) region. In particular, the tropical cold point tropopause, defined as minimum level in the tropical UTLS temperature profile (Highwood & Hoskins, 1998; Seidel et al., 2001; Pan et al., 2018), acts like a "cold trap" to "freeze-dry" air carried into the lower stratosphere by the Brewer-Dobson circulation (Brewer, 1949; Holton & Gettelman, 2001; Dessler, 2002). Warmer cold point temperatures have been strongly linked to increased moisture in the lower stratosphere, and likewise colder cold point temperatures with a drier lower stratosphere, across many different time scales (Randel & Jensen, 2013; Zhou et al., 2001b; Randel & Park, 2019; Avery et al., 2017). Changes in the cold point temperature are therefore strongly coupled with changes in the climate.

Deep convection, particularly that which overshoots the cold point tropopause, may play a strong role in determining the cold point temperature and height. Entrainment between overshooting tops and the UTLS may lower the cold point temperature (Kuang & Bretherton, 2004; Chae et al., 2011; Randel & Park, 2019) and in turn allow convection to penetrate even higher (Gettelman et al., 2002). One example of this process was identified by Proud and Bachmeier (2021), in which an anomalously cold tropopause likely caused an extreme convective event with the coldest cloud top temperatures on record. Cold anomalies in the

cold point temperatures have also been associated with changes in convection from Madden-Julian Oscillation and El Niño-Southern Oscillation cycles (Hatsushika & Yamazaki, 2001; Zhou & Holton, 2002; Liou & Ravindra Babu, 2020) as well as the seasonal shift in the Intertropical Convergence Zone (Jain et al., 2011). Suneeth et al. (2017) also found that the cold point became higher and cooler after the respective diurnal peak in convection over both land and ocean regions. Still, the role of overshooting convection specifically in setting the cold point has not been adequately investigated.

Another possible control on the cold point temperature and height is radiative lofting of cirrus clouds in the Tropical Tropopause Layer (TTL, ∼14–18 km), the transition region between the upper troposphere and lower stratosphere (Fueglistaler et al., 2009). Very thin cirrus near the cold point tropopause have a slight radiative heating effect that can gradually loft the cirrus layer (Jensen et al., 1996b; Fueglistaler et al., 2009; Ali et al., 2020). Corti et al. (2006) suggested that this lifting provides a significant fraction of the net mass transport from the TTL to the lower stratosphere. Furthermore, Durran et al. (2009) found that rising motion can in turn cool the layers above and below the cirrus clouds. Thin cirrus can also provide direct cooling through a net radiative cooling effect when they are located above convective anvils (Hartmann et al., 2001). The radiative lofting of thin cirrus may thus act to cool the tropopause, setting the cold point temperature.

A more thorough understanding of how overshooting convection influences the cold point temperature is necessary to understand how the cold point may change in a future warmed climate. Several long-term trends in the cold point have already been identified, including a cooling trend over a 25-year period (Zhou et al., 2001a) and temperature variations linked to an areal expansion of the tropical warm pool (Xie et al., 2015). Additionally, extreme convective events with very cold cloud top temperatures stemming from anomalously cool cold points may be increasing in frequency (Proud & Bachmeier, 2021). Changes in overshooting convection in a warmed climate may drive these changes in the cold point temperature. Modeling studies of perturbed climates have found that warmer sea surface temperatures lead to more intense convection and more frequent overshoots, especially over oceans (Aumann et

al., 2018; Cheng et al., 2022; Wu et al., 2023). It is thus important to understand how cold point-overshooting convection influences the cold point temperature in the current climate so that we can better predict how the cold point temperature, and thus lower stratospheric moisture, may change in a future warmed climate.

To determine the relative importance of overshooting convection and cirrus lofting in setting the cold point tropopause, global storm-resolving models (GSRMs) are promising tools. GSRMs are global cloud-resolving models with sufficiently fine horizontal grid spacings (<5km) to explicitly resolve deep convection. By avoiding parameterized deep convection, GSRMs can potentially eliminate many of the biases in simulating convection that global climate models (GCMs) typically have, such as the diurnal cycle of convection over land peaking too early in the day (e.g., Bechtold et al., 2004; Duda & Gallus, 2013). The horizontal grid spacing in GSRMs may be small enough to capture convective overshoots (radii of ∼3 km; Xian & Fu, 2015) that are not resolved by typical GCM grid spacings of ∼25–200km. GSRM vertical grid spacings are typically ∼500 m in the TTL, marginally fine enough to represent cirrus formation processes. Compared to in situ and remote observations which may be coarse or limited in spatiotemporal resolution, GSRMs can provide a complete picture over the atmosphere over space and time and across all parts of the diurnal cycle of convection.

However, the full potential of GSRMs has not yet been realized. A recent intercomparison of GSRMs from the DYnamics of the Atmospheric general circulation Modeled On Non-hydrostatic Domains (DYAMOND) initiative, detailed in Stevens et al. (2019), provided insight into the range in performance of current GSRMs. Studies analyzing the DYAMOND model output identified significant inter-model differences, particularly in the model microphysics and dynamics. Still, these studies also demonstrated that the DYAMOND GSRMs can reasonably reproduce the overall character of tropical deep convection, radiative effects of cirrus clouds, and zonal-mean water vapor (Judt et al., 2021; Nugent et al., 2022; Turbeville et al., 2022; Dauhut & Hohenegger, 2022) and thus can provide insight into processes in the real atmosphere.

The goal of this paper is to assess whether overshooting convection or cirrus lofting may

play a larger role in setting cold point temperature and height in GSRMs using the second (boreal winter) phase of the DYAMOND intercomparison (DYAMOND2; Duras et al., 2021). The rest of this paper is organized as follows. Section 4.2 details the DYAMOND2 models, observations, and reanalysis used in this study. Section 4.3 describes the background cold point tropopause in the models and observations. In Section 4.4, we adapt the brightness temperature proxy from Nugent and Bretherton (2023) to the GSRMs to compare the simulated geographic distribution of cold point overshoots to observations. In Section 4.5, we evaluate the simulated frequency and distribution of the radiatively active cold point cirrus capable of lofting the cold point. Section 4.6 discusses how these mechanisms, cold point-overshooting convection and radiative cirrus lofting, may contribute to the background cold point temperature in both models and observations. Finally, we summarize this paper and present our conclusions in Section 4.7.

4.2 Models and Data Sets

4.2.1 DYAMOND2 Models

The second phase of the DYAMOND initiative, DYAMOND2 (Duras et al., 2021), continues the original DYAMOND initiative described in Stevens et al. (2019) for boreal winter. Twelve GSRMs, all with sub-5 km horizontal grid spacings and explicit (nonparameterized) deep convection, were initialized with the same meteorological analysis and run freely for 40 days from January 20 to March 1, 2020. This period includes a 10-day spinup period, so we only include model output from January 30 onward in our analysis. In addition to the fine horizontal grid spacing, the DYAMOND2 GSRMs have vertical grid spacings of 250–500 m in the UTLS, 15 minute 2D output, and 3 hourly 3D output. Most GSRMs use one moment microphysics schemes while SCREAM uses the two-moment Predicted Particle Properties (P3) scheme (Caldwell et al., 2021; Morrison & Milbrandt, 2015).

We primarily use five of the DYAMOND2 models in this study given in Table 4.1: ICON, GEOS, gSAM, SCREAM, and X-SHiELD. We focus on the convectively active tropics during

boreal winter and limit analysis to 30°S–10°N. To more easily manage output volume for a detailed analysis of select 3D variables, we use representative $10° \times 10°$ regions described in Section 4.2.2.

Table 4.1: List of DYAMOND2 Models

Abbreviation	Model name	Reference(s)	Horiz. grid spacing (km)	Vertical levels
ICON	Icosahedral Non-hydrostatic Model	[Zängl et al. (2015), Klocke et al. (2017)]	2.5	90
gSAM	Global System for Atmospheric Modeling	Khairoutdinov et al. (2022)	4.3	74
GEOS	Goddard Earth Observing System	[Putman and Lin (2007), Putman and Suarez (2011), Putman (2021)]	3.25	181
SCREAM	Simple Cloud-Resolving E3SM Atmospheric Model	Caldwell et al. (2021)	3.25	128
X-SHiELD	eXperimental System for High-resolution prediction on Earth-to-Local Domains	[Lin (2004), Harris et al. (2020), Harris et al. (2023)]	3.25	79

Note. DYAMOND2 models used in this study.

4.2.2 Analysis Regions

Following Nugent et al. (2022) and Turbeville et al. (2022), we use four representative $10° \times 10°$ latitude-longitude regions to sample land and ocean areas across the tropics for a more thorough analysis of some GSRM outputs. We use two regions that are subsets of the larger study areas used in Nugent and Bretherton (2023): Amazonia (AMZ) and the South Pacific Convergence Zone (SPC). We also study another continental region, South-Central Africa (SCA), and an oceanic region over the Timor Sea (TIM) in the Maritime Continent. These regions and their coordinates are shown in Figure 4.1. These areas encompass "hot spots" of tropical convection during boreal winter (e.g., Liu & Zipser, 2005; Zipser et al., 2006; Li et al., 2022).

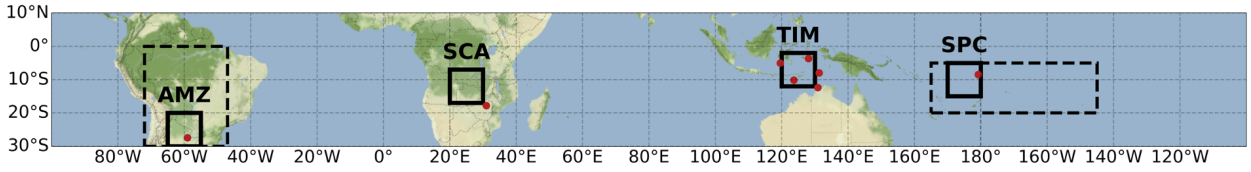

Figure 4.1: Map of the $10° \times 10°$ analysis regions within the tropics. From left to right: Amazonia (AMZ; 65°W–55°W, 30°S–20°S), South-Central Africa (SCA; 20°E–30°E, 17°S–7°S), Timor Sea (TIM; 120°E–130°E, 12°S–2°S), and the South Pacific Convergence Zone (SPC; 170°–180°E, 15°S–5°S). Red dots show the station locations of the IGRA soundings used. The dashed boxes depict the larger AMZ and SPC regions used in Nugent and Bretherton (2023).

4.2.3 Observations and Reanalysis

The DYAMOND models are not nudged towards observations or reanalysis during the model run so they do not necessarily reproduce the actual weather systems that occurred during that time period. We instead use observations and reanalysis to evaluate the fidelity of the GSRMs in a statistical sense.

We use ice water content (IWC) from the joint radar/lidar DARDAR-CLOUD v3.10 data set (Delanoë, 2023), which has a horizontal footprint of 1.4 km and 60 m vertical resolution. The DARDAR product merges CloudSat radar and CALIPSO lidar retrievals from the NASA A-Train, which crosses the equator daily at 01:30 and 13:30 local time. The DARDAR-detected "ice" inherently includes all frozen hydrometeors while all models except SCREAM distinguish between cloud ice, snow, and graupel; we use "frozen water" when referring to the sum of all frozen hydrometeors in the GSRM output to avoid confusion. We convert the DARDAR IWC to a mixing ratio using reference densities from a standard tropical atmosphere profile. For brightness temperature data, we use infrared brightness temperatures derived from geostationary satellites in the NCEP/CPC L3 Half Hourly 4 km Global (60S–60N) Merged IR V1 (GPM_MERGIR) data set (Janowiak et al., 2017). This data set has a 4 km horizontal resolution, comparable to the DYAMOND GSRMs, and a temporal resolution of 30 minutes.

We compare the GSRM temperature output to hourly temperature profiles from the ECMWF Reanalysis v5 (ERA5) reanalysis (Hersbach et al., 2020). The ERA5 data is mapped to a $0.25° \times 0.25°$ grid and has 137 vertical levels, corresponding to a vertical resolution of 300–400 m in the UTLS (Hersbach et al., 2017). Using the ERA5 reanalysis as an observational comparison allows us to more directly compare these model results to the climatology from Nugent and Bretherton (2023). To supplement the model-observations comparison for temperature, we also examine radiosonde data from the Integrated Global Radiosonde Archive (IGRA) for several stations located within or just outside of the analysis regions. We use a total of seven stations: five in TIM (station IDs 97372, 97724, 94120, 97900, 97180), one in SCA (67774), one in the SPC (91643), and one in AMZ (87155). We use the mean cold point temperature and height across all stations within each region to compare to the GSRMs and reanalysis.

To maximize the sample size available for observational comparisons, we primarily use DARDAR, ERA5, and GPM_MERGIR data from December-January-February (DJF) 2007–2010, following Nugent and Bretherton (2023); after 2010, CloudSat only operated during the daytime. However, for the frequency maps of cold point overshoots in Section 4.4.2, we use reanalysis from February 2020 for a more direct comparison with the DYAMOND2 output. Except for the radiosonde station in the SCA region, all sounding profiles are from February 2020. The SCA station (67774) record ended in 2017, so we use February 2002 instead which had similar climatological conditions to 2020. For most analysis, we resample the ERA5 data to match the 3D temporal output frequency (3 hourly) of the DYAMOND2 GSRMs.

4.3 Cold Point Tropopause

We define the cold point tropopause using the level of the minimum temperature on a $0.25° \times 0.25°$ grid as in Nugent and Bretherton (2023). To match the DYAMOND models to the reanalysis, we first take the mean temperature profile over a $0.25° \times 0.25°$ area and then calculate the cold point from the coarsened grid. The uncertainties in the ERA5 reanalysis

temperatures are described more thoroughly in Nugent and Bretherton (2023), but we expect an uncertainty around ±120—200 m (Hoffmann & Spang, 2022) in the tropopause height and a slight warm bias of < 0.5 K in the cold point temperature (Tegtmeier et al., 2020a).

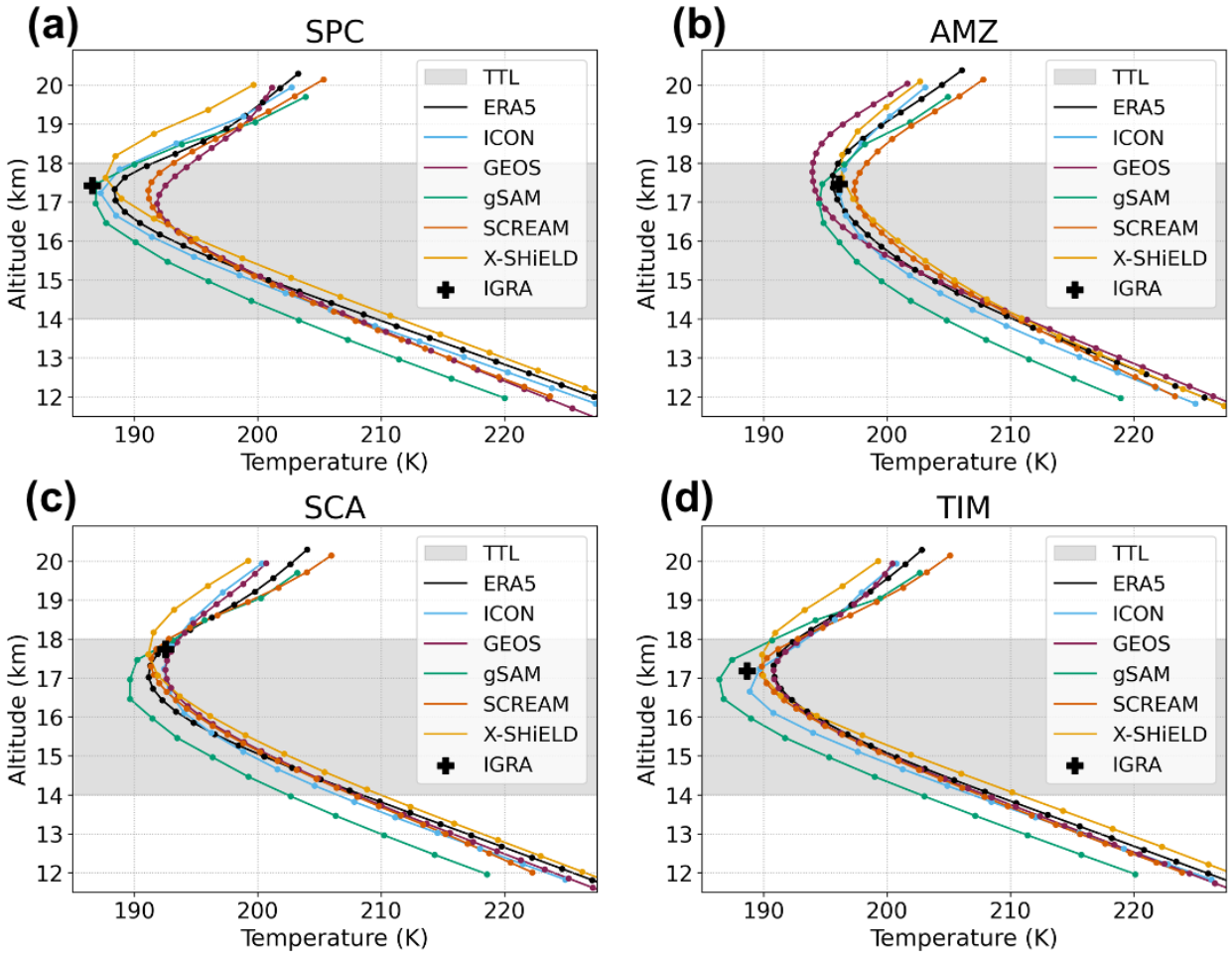

Figure 4.2: Time- and area-mean temperature profiles for the DYAMOND2 GSRMs and ERA5 reanalysis in the (a) AMZ, (b) SPC, (c) SCA, and (d) TIM regions. The TTL is shaded in grey. Crosses mark the mean cold point height and temperature from IGRA soundings in each region.

Figure 4.2 shows the time- and area-mean UTLS temperature profiles for the four analysis regions for the DYAMOND models and ERA5 reanalysis. The mean cold point temperature

and height from available radiosonde data (black crosses; see Figure 4.1 for station locations) is also included for further comparison. Note that IGRA data is available from five locations in and around the TIM region, but only one location in each of the other regions; the small sample size of radiosonde profiles in SPC, AMZ, and SCA means that the mean cold points from the radiosondes may not be entirely representative of the region as a whole.

The GSRM temperature profiles generally scatter around the ERA5 profiles with cold points within 5 K and 0.5 km of the reanalysis. However, the sounding cold points are cooler than most of the GSRMs in the SPC and TIM and are higher than the cold points in SCA for all but X-SHiELD. gSAM consistently has the lowest and coldest mean cold points of all the GSRMs, while X-SHiELD is generally the highest; the other GSRMs do not have clear trends between regions. Both the GSRMs and the reanalysis have good agreement with the mean IGRA sounding cold points in AMZ (Figure 4.2 b).

We compare both the temperature and height of the cold point across the tropics over the 30-day period between ERA5 and the GSRMs in Figure 4.3. The mean cold point temperatures are remarkably similar between the models and the observations. All GSRMs simulate the coldest cold points over the Pacific warm pool, consistent with the observations. However, cold points over the oceans tend to be slightly colder in the GSRMs, although this may be partially due to the slight warm bias (<0.5 K) in the ERA5 climatological cold point (see Section 4.2.3). There is more variation in the cold point heights between the models, although within each model the heights are more consistent geographically than the temperatures. X-SHiELD (Figure 4.3 k) has the highest cold points while ICON, GEOS, and SCREAM are in good agreement with the ERA5 cold point heights. As in Figure 4.2, gSAM (Figure 4.3 g–h) simulates the coldest and the lowest cold points of the DYAMOND2 GSRMs. However, gSAM does not have the highest cold point pressures of the models (not shown). Unlike the other DYAMOND2 models shown here, gSAM is an anelastic model (Khairoutdinov et al., 2022); the additional approximations in the model equations cause the UTLS temperature profile in height space to look different from the other models.

In ERA5 and the GSRMs, there is also a strong positive association between higher

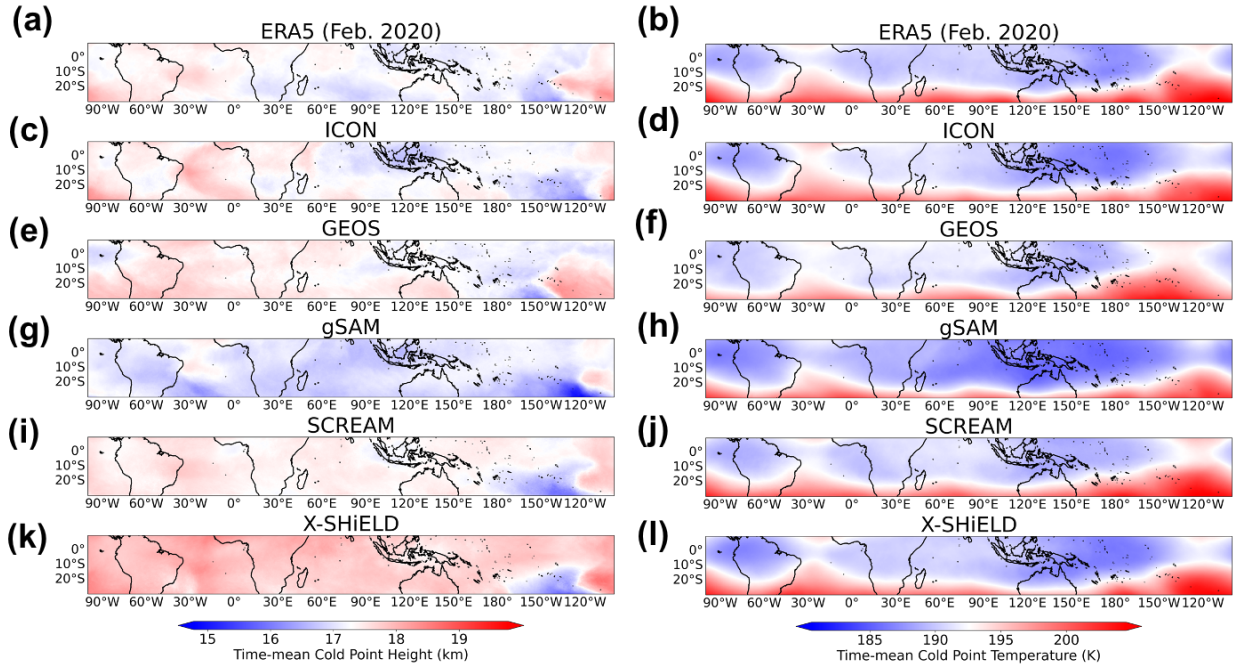

Figure 4.3: Time-mean 0.25° cold point height (left) and temperature (right) for (a)–(b) ERA5, (c)–(d) ICON, (e)–(f), GEOS, (g)–(h) gSAM, (i)–(j) SCREAM, and (k)–(l) X-SHiELD. The color map is centered on the tropics-mean ERA5 cold point values such that blue (red) colors indicate areas of lower/colder (higher/warmer) cold points.

cold point heights (>18 km) and warmer cold point temperatures (>200 K) from 20°S–30°S between ∼120°W and 100°W (lower right corner of each panel in Figure 4.3). This feature is surprising given that warmer temperatures generally correspond to lower heights in the troposphere and is likely due to double tropopause events. Our method for identifying the cold point tropopause simply takes the level of the minimum UTLS temperature, which in some cases may identify the higher (secondary) tropopause as the cold point if it is marginally colder than the primary tropopause.

Overall, the GSRMs reasonably reproduce the observed cold point temperatures and heights, but with some key inter-model differences across regions. These differences underscore the importance of using cold point-relative metrics to identify cold point cirrus and overshoots rather than fixed altitude levels.

4.4 Cold Point-Overshooting Convection

4.4.1 Brightness Temperature Proxy for Cold Point Overshoots

To identify cold point-overshooting convection in the GSRMs, we adapt the brightness temperature proxy developed in Nugent and Bretherton (2023). Since brightness temperature was not a saved output in any of the models, we estimate the broadband brightness temperature from model output of outgoing longwave radiation (OLR) using the inverse Planck function: $OLR = \sigma T_b^4$. The resultant broadband brightness temperature is not the same as the GPM_MERGIR IR brightness temperatures used in Nugent and Bretherton (2023) and the observational comparisons here, but we expect it to be close in cloudy regions at low OLR/low T_b. We calibrate the proxy as before by binning frozen water mixing ratios by $T_b - T_{cp}$ at levels relative to the local 0.25° cold point height (z_{cp}) in the GSRMs, combining methods similar to Dauhut and Hohenegger (2022) and Pan and Munchak (2011). Recalibrating the observed proxy from Nugent and Bretherton (2023) for the GSRMs ensures that any differences between the estimated and actual T_b in the models are accounted for. ICON and gSAM did not save the full 3D profiles of snow or graupel; since we cannot calculate

the total frozen water mixing ratio that would be equivalent to the DARDAR-observed ice, we omit these two models from our calibration process. The identified cold point overshoots in ICON and gSAM therefore may not be perfectly representative of the actual simulated overshoots. For the observations, we use the DJF 2007–2010 observational data from the larger SPC and AMZ regions used in Nugent and Bretherton (2023); the limited sampling from the DARDAR instrument means that the $10° \times 10°$ regions do not have sufficient sample size to capture the actual relationship between frozen water and $T_b - T_{cp}$, even over this time period.

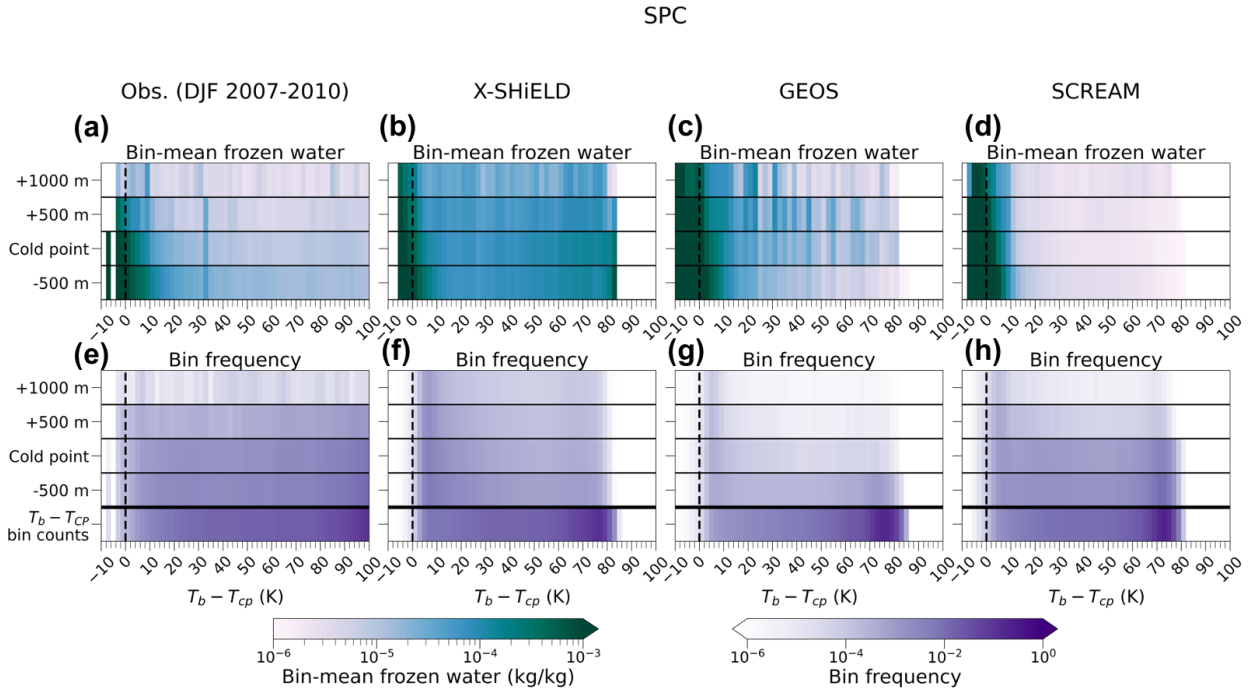

Figure 4.4: Cold point-relative frozen water binned by $T_b - T_{cp}$ in the SPC region for (a) DARDAR observations, (b) X-SHiELD, (c) GEOS, and (d) SCREAM. The top row of plots shows the bin-mean cloud-conditional frozen water mixing ratio at 500 m below to 1000 m above the local cold point height. The bottom row of plots shows the bin counts conditioned on when (a) DARDAR detects ice or (b)–(d) the GSRM frozen water exceeds a lower threshold of 1×10^{-6} kg/kg. The total brightness temperature bin counts are shown below the thick black line in the bottom row of plots. The dashed lines mark where the brightness temperature equals the cold point temperature. The bin width is 2 K.

The bin-mean cloud-conditional frozen water and $T_b - T_{cp}$ bin counts for DARDAR observations, X-SHiELD, GEOS, and SCREAM are shown in Figure 4.4 for the SPC (see Figure B.1 for the AMZ). There are substantial inter-model differences in the cold point-relative frozen water mixing ratios. Above $T_b = T_{cp}$ (dashed lines in Figure 4.4), the models simulate vastly different amounts of frozen water from each other and from the observations. SCREAM has very little frozen water outside of the areas of deep convection with low T_b, both in terms of amount and frequency, while X-SHiELD has too much of both. GEOS has more frozen water than the observations at z_{cp} and $z_{cp} + 500$ m, but not as much as in X-SHiELD. In both GEOS and SCREAM, there is much less frozen water near the cold point at higher T_b than in the observations, suggesting that thin cirrus located above the cold point are underrepresented in these GSRMs. There is little regional variation in the binned frozen water between the SPC (Figure 4.4) and AMZ (Figure B.1). The inter-model differences far exceed the regional differences, as Nugent et al. (2022) and Turbeville et al. (2022) found for the DYAMOND1 models. Despite these inter-model differences, the mean frozen water at $z_{cp} + 500$ m increases considerably below $T_b = T_{cp}$ in the GSRMs as it does in the observations. The pronounced increase in mean frozen water when $T_b < T_{cp}$ suggests that cold point overshoots occur below this threshold.

In Figure 4.5, we restrict the DARDAR observations to pixels where both the CloudSat radar and CALIPSO lidar detect ice as in Nugent and Bretherton (2023). Since we cannot restrict the GSRM output by instrument type, we instead set a minimum frozen water mixing ratio threshold of 5×10^{-5} kg/kg. This mixing ratio approximately corresponds to an IWC of 5×10^{-6} kg/m^3 near the cold point, which falls within the range of mean IWC observed in overshooting tops in Iwasaki et al. (2010). These restrictions should exclude thin cirrus that could not be detected by the radar and thus limit the analysis to cirrus likely related to convection and cold point overshooting tops. GEOS and SCREAM indeed have much less frozen water above the cold point at higher T_b, but the bin counts decrease almost uniformly in X-SHiELD (Figure 4.5b), which further suggests that thick cirrus with anomalously high frozen water content exist above the cold point at high T_b in X-SHiELD. As with Figure 4.4,

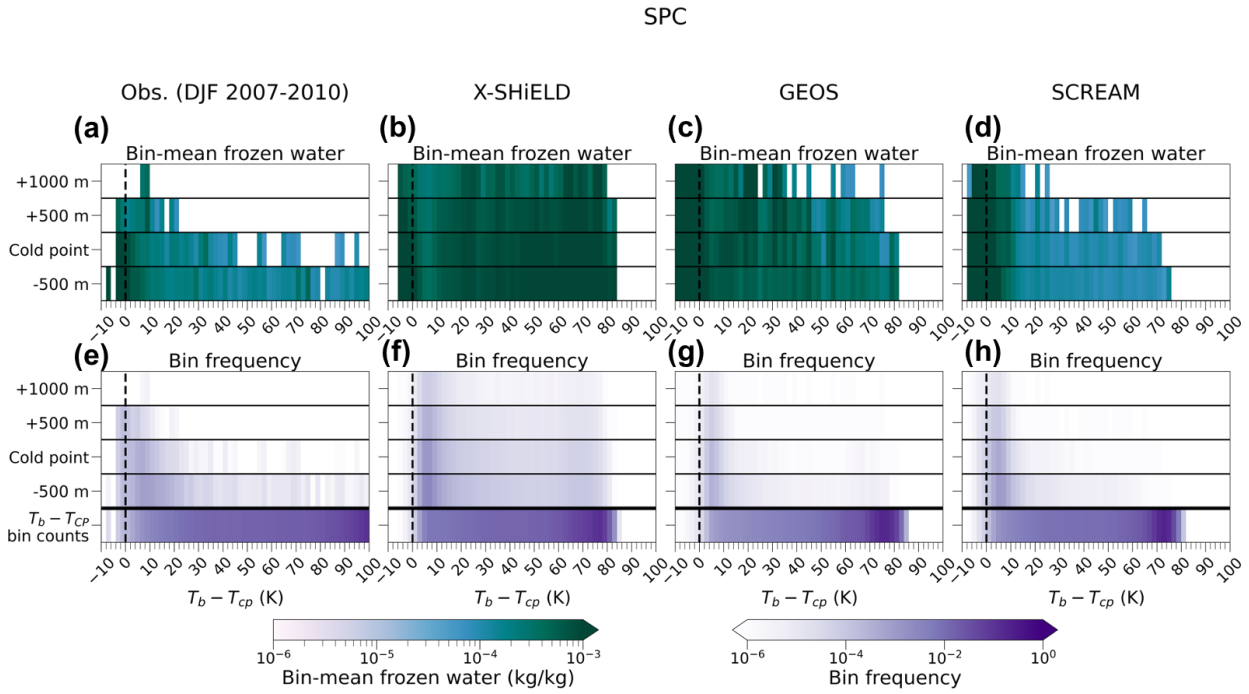

Figure 4.5: As in Figure 4.4, but restricted to (a) DARDAR pixels detected by both the radar and lidar or (b)–(d) GSRM grid points where the mixing ratio at that level exceeds 5×10^{-5} kg/kg.

there are few regional differences between models in the binned plots (see Figure B.2 for the AMZ). One notable difference is that in GEOS, similar to X-SHiELD, there are still bins with mean cloud ice above 5×10^{-5} kg/kg at $z_{cp} + 1000$ m for high T_b.

As in Nugent and Bretherton (2023), we calculate the fraction of convective cirrus and "other stratospheric cirrus." In the DARDAR observations, we calculate the fraction of retrievals with ice detectable by both the radar and lidar for convective cirrus fraction and lidar-only retrievals for other stratospheric cirrus. In the GSRMs, we use the fraction of columns with frozen water mixing ratios $\geq 5 \times 10^{-5}$ kg/kg to find the convective cirrus fraction and the fraction of columns with frozen water mixing ratios between 1×10^{-6} kg/kg and 5×10^{-5} kg/kg for other stratospheric cirrus. GSRMs simulate about 5 times less other stratospheric cirrus over land in the AMZ than in the observations (∼0.5% vs. 2.6%), but

more convective cirrus (0.04%–0.07% vs. 0.01%). The intermodel spread in other cirrus is much larger over oceans in the SPC, ranging from 0.08% in GEOS to 1.5% in X-SHiELD vs. 2.4% in the observations. While the other stratospheric cirrus fraction in the SPC is closest to the observations in X-SHiELD, the convective cirrus fraction is 5 times larger (0.2% vs. 0.04%). Overall, thin cirrus above the cold point are underrepresented in the GSRMs except for X-SHiELD, which simulates too much frozen water everywhere near the cold point.

Joint histograms of T_b and T_{cp} are shown in Figure 4.6 for the SPC and Figure 4.7 for the AMZ. For the observations, the ERA5 and GPM_MERGIR data is not restricted to the times and locations of DARDAR retrievals and thus are directly comparable to the GSRM histograms. In the observations and GSRMs, the frequency of values with $T_b < T_{cp}$ (below the solid line in Figures 4.6–4.7; see percentages on the panels) is similar between the $10° \times 10°$ ocean and land regions. The general shape of the distributions differs between regions, however. The distribution is wider in the AMZ, meaning there is a larger range in cold point temperatures over land. The distribution in the AMZ bulges slightly along the $T_b = T_{cp}$ line towards low T_b and low T_{cp} (175–200 K and 180–185 km, respectively, in Figure 4.7a). This small "tail" corresponds to the more frequent deep convection that does not reach the cold point. It is not apparent in the SPC histograms (Figure 4.6), consistent with the generally less intense deep convection observed over oceans than land regions (e.g., Liu & Zipser, 2005; Zipser et al., 2006). These observed regional patterns are reproduced by all of the GSRMs except GEOS (Figure 4.6c), which does not have the low T_b / low T_{cp} tail in the SPC. Instead, GEOS has a tail on the opposite side with low T_b but high T_{cp} ($\sim$197–200 K).

Overall, we conclude that $T_b < T_{cp}$ is an effective proxy for identifying likely cold point overshoots in the GSRMs (GEOS, SCREAM, and X-SHiELD) as well as in the observations.

4.4.2 Geographic Distribution of Cold Point Overshoots

The 3 hourly temporal resolution and 30-day period of the DYAMOND models results in a much smaller sample size than the ERA5/GPM_MERGIR climatology from Nugent and Bretherton (2023). Therefore, in Figure 4.8 we evaluate the frequency of cold point over-

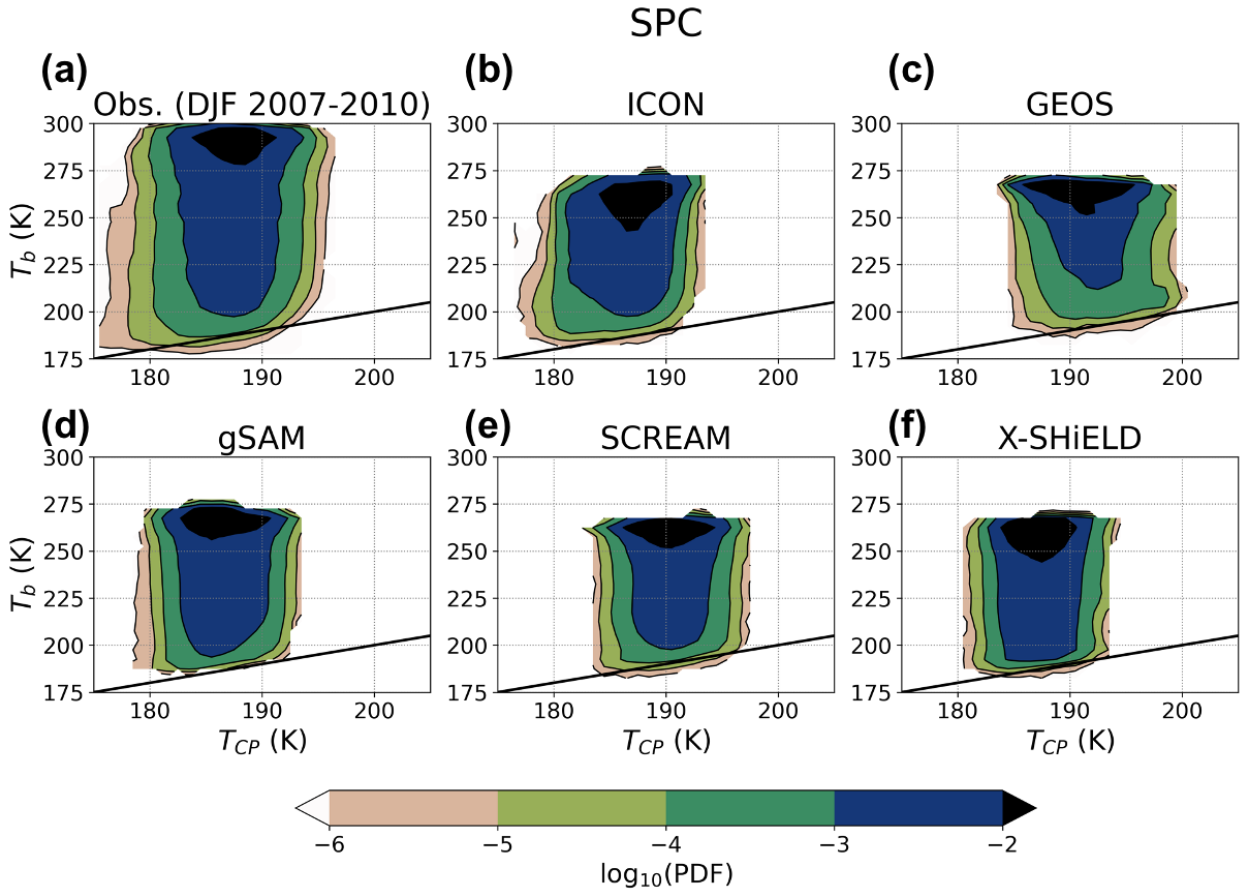

Figure 4.6: Joint brightness temperature-cold point histograms for all data points in the SPC region in (a) ERA5/GPM_MERGIR observations, (b) GEOS, (c) SCREAM, (d) X-SHiELD, (e) gSAM, and (f) ICON. The solid lines mark where the brightness temperature equals the cold point.

shoots within $5° \times 5°$ boxes across the tropics. Each $5° \times 5°$ box contains approximately 13,000 to 48,000 grid cells. We compute the $5° \times 5°$ frequencies by summing the number of instances of cold point overshoots within each box and dividing by the total number of profiles (i.e., the number of grid cells times the number of time steps). To match the DYAMOND output for a fair comparison, we use ERA5 cold point and GPM_MERGIR brightness temperature data from February 2020 sampled every 3 hours.

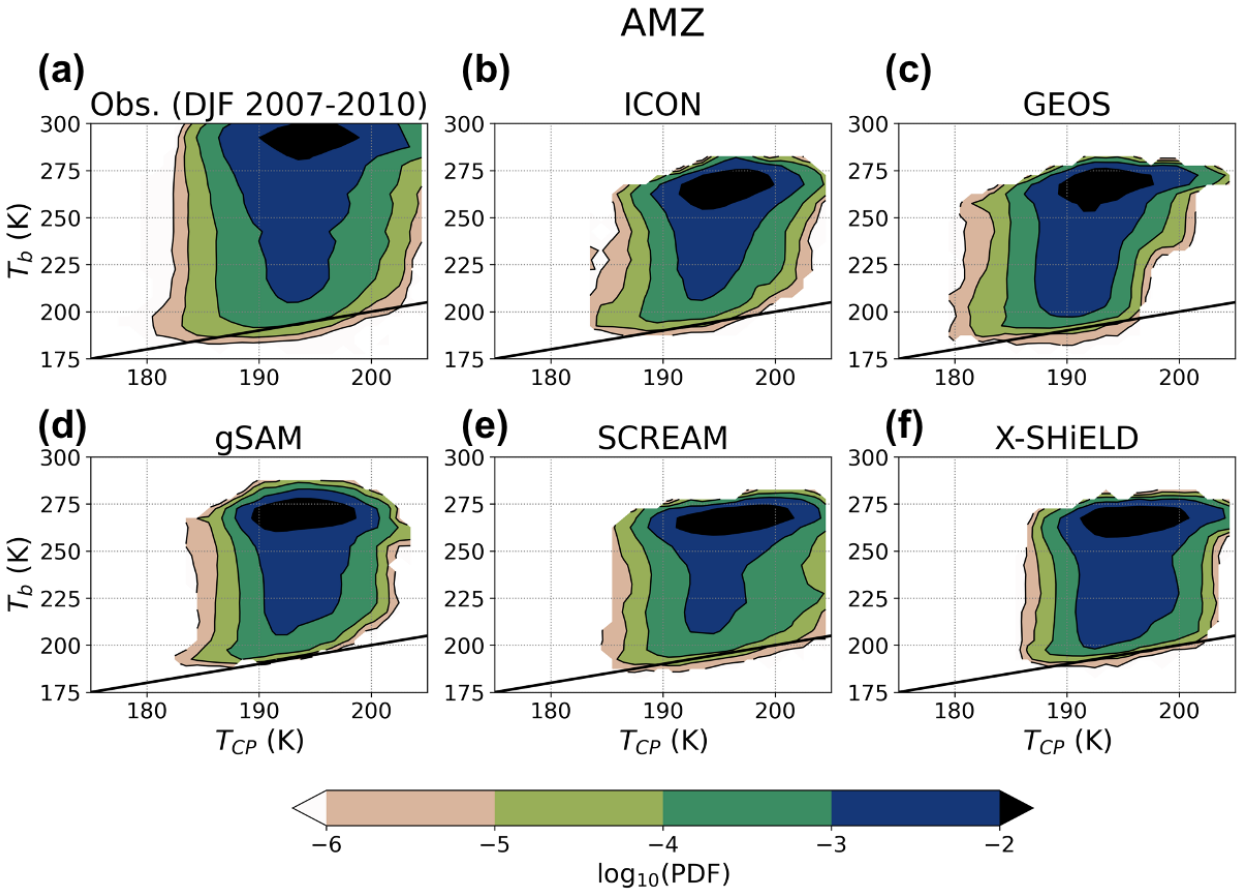

Figure 4.7: As in Figure 4.6, but for the AMZ region.

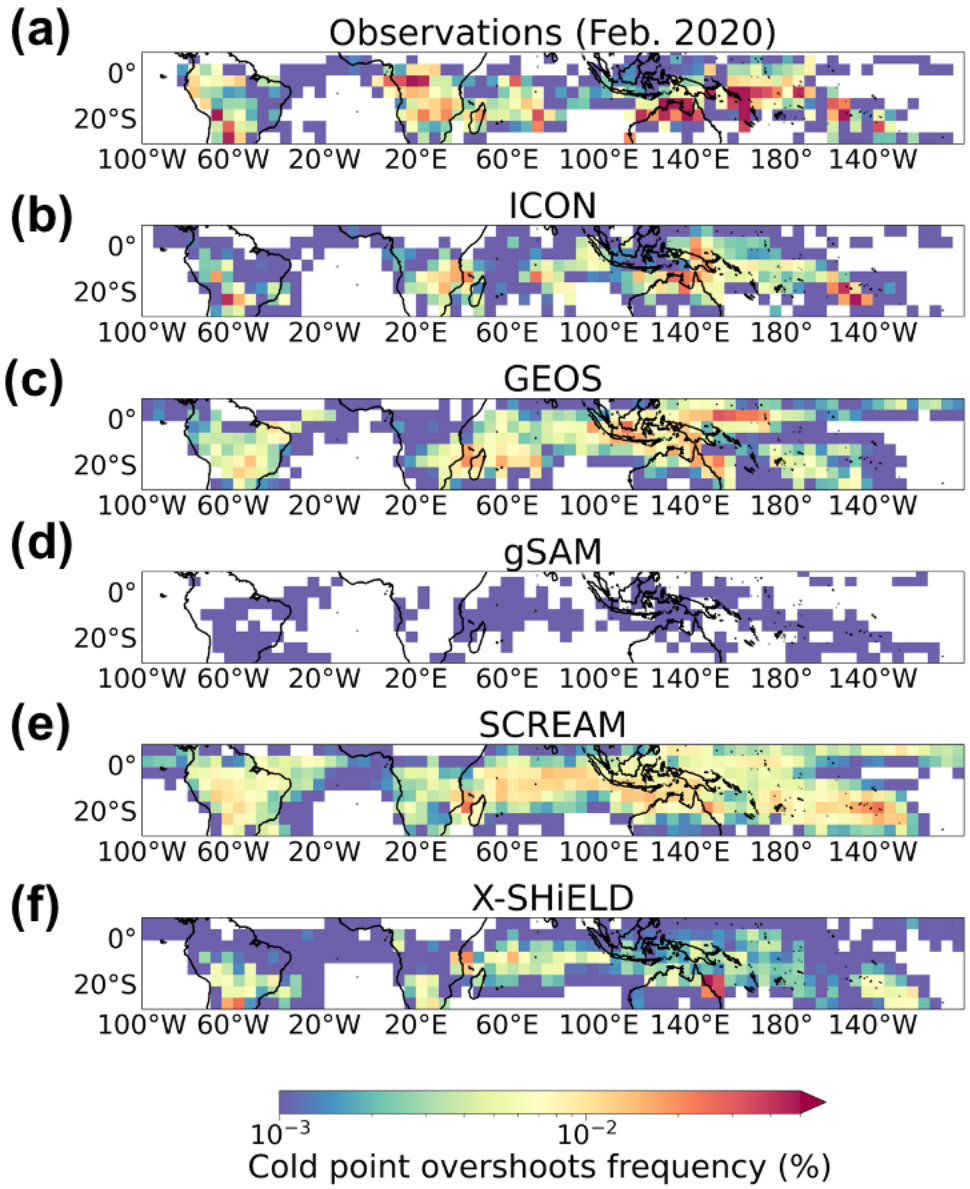

Figure 4.8: Frequency of cold point overshoots in the 30-day period within $5° \times 5°$ latitude-longitude boxes for (a) ERA5/GPM_MERGIR observations and (b) ICON, (c) SCREAM, (d) GEOS, (e) gSAM, and (f) X-SHiELD GSRMs. The observations have been sampled every 3 hours to match the temporal resolution of the DYAMOND GSRMs. The apparent lack of cold point overshoots in gSAM should be disregarded; see the text for details.

Except for gSAM, the geographic distribution of cold point overshoots shown in Figure

4.8 is strikingly similar between the GSRMs and the observations. Therefore, despite the inter-model differences in cold point temperatures and deep convection, the models simulate cold point overshoots in a very similar manner. However, the slight favoring of land regions over ocean regions in observed cold point overshoots is not reproduced by all of the GSRMs. SCREAM, and to a lesser extent X-SHiELD, tend to simulate cold point overshoots too often over oceans relative to the amount they simulate over land regions. Deep convection, especially updraft speeds, may therefore be too vigorous over the oceans in these GSRMs, allowing convection to penetrate the cold point too frequently.

The observations reveal the hot spots in overshooting convection over Africa, South America, the Maritime Continent, and the Pacific Warm Pool expected from previous studies (e.g., Liu & Zipser, 2005; Zipser et al., 2006; Takahashi & Luo, 2014; Li et al., 2022). Cold point overshoots favor the land areas overall, consistent with the climatology from Nugent and Bretherton (2023), although many of the boxes with $\geq$10% frequency occur over ocean areas. ICON and GEOS reproduce this pattern well with the expected hot spots, especially over the Maritime Continent. SCREAM also simulates more overshoots over oceans than land, but cold point overshoots occur less often than in the other models, even in the highest frequency boxes. The lower frequency could be caused by the "popcorn"-like texture of simulated convection in SCREAM (Caldwell et al., 2021) since the simulated overshoots may not cover as much area as in the other GSRMs. X-SHiELD simulates nearly equal amounts of cold point overshoots over land and oceans, consistent with recent findings from Harris et al. (2023) who used a similar configuration of X-SHiELD.

The apparent lack of cold point overshoots in gSAM in Figure 4.8e is more likely due the $T_b < T_{cp}$ proxy than the performance of gSAM itself. Because cloud ice is the only radiatively active frozen hydrometeor in gSAM, the brightness temperature estimated from OLR may not reflect the vertical structure of deep convection. This difference would make it more difficult for clouds to have $T_b < T_{cp}$ (note the lack of grid points with $T_b < T_{cp}$ in Figures 4.6–4.7 d) and could allow significant amounts of ice above the cold point when $T_b > T_{cp}$. However, we cannot properly adjust the brightness temperature proxy for gSAM

without the full 3D profiles of snow or graupel. The apparent underestimation of cold point overshoots in gSAM in Figure 4.8d should therefore be disregarded; more work is needed to determine how often cold point overshoots atually occur in gSAM.

In the GSRMs and observations, cold point overshoots seem to be related to the mean cold point temperature and height. Areas of frequent cold point overshoots in Figure 4.8 generally coincide with areas of colder mean cold points (Figure 4.3). Comparing the models to the observations also reveals a relationship between cold point overshoots and the time-mean cold point height. For example, in SCREAM and X-SHiELD, the mean cold point heights (Figure 4.3) are quite consistent across the Indian Ocean and Pacific warm pool, but in ERA5 the cold point heights are lower over the Indian Ocean than the Pacific warm pool. This difference is consistent with the increased cold point-overshooting convection over the Indian Ocean in SCREAM and X-SHiELD compared to the observations (Figure 4.8). Likewise, ICON and the observations have there fewer cold point overshoots over the Maritime Continent than the rest of the GSRMs (Figure 4.8), which corresponds to a pocket of lower cold point heights in the Maritime Continent for ICON and the observations (Figure 4.3). These patterns suggest that areas of more frequent cold point overshoots are associated with both colder and higher mean cold points.

Overall, the GSRMs reproduce the observed distribution of cold point-overshooting convection and thus can be used to study overshooting convection in the real world.

4.5 Radiative Lofting of Cold Point Cirrus

4.5.1 Defining Radiatively Active Cold Point Cirrus

To evaluate the potential for radiative lofting of cirrus near the cold point in the GSRMs, we must identify cirrus in the DYAMOND2 output that can produce a radiative heating rate strong enough to lead to net upward motion. However, vertical profiles of heating rates or optical depth were not commonly saved model output for the DYAMOND2 GSRMs. We therefore identify "radiatively active cold point cirrus" (hereafter "RACP cirrus") using the

ice mixing ratio alone by finding the approximate cloud ice concentration needed for a cirrus cloud near the cold point to have a radiative heating rate exceeding its ice fall velocity. An ice crystal with a radius of 10.6 μm, typical of cirrus near the cold point (Krämer et al., 2016), would have a fall velocity of 20 mm/s (Dinh et al., 2010). Assuming an environmental lapse rate of 6.5 K/km, a radiative heating rate of 5.6 K/day is needed to have net upward motion.

To calculate the critical ice concentration, we consider an idealized cirrus cloud near the cold point at 17 km altitude with a temperature of 195 K and a geometric thickness of 1 km. We assume the incident radiation at the bottom of the cloud is near that of a clear sky region in the tropics at 260 W/m^2. To achieve a radiative heating rate of 5.6 K/day, such a cloud would need an optical depth of $\sim$0.1, corresponding to a cloud ice mixing ratio (q_i) of 2×10^{-6} kg/kg. Therefore, we define RACP cirrus in the GSRMs as columns near the cold point with a cloud ice concentration of $> 2 \times 10^{-6}$ kg/kg.

4.5.2 Frequency of Radiatively Active Cold Point Cirrus

Figure 4.9 shows histograms of cold point-relative cloud ice $> 2 \times 10^{-6}$ kg/kg for the GSRMs in the SPC. For the observational comparison, we use DARDAR data from February 2007–2010. On average, each $5^\circ \times 5^\circ$ box includes a total of $\sim$19,000 DARDAR retrievals across the entire time period, comparable to the number of grid points for the GSRMs during February 2020. Here, we plot the cloud ice distributions at the z_{cp}-relative levels used in Figures 4.4–4.5 as well as $z_{cp} - 1000$ m to get an idea of how the RACP cirrus frequency changes with height around the cold point. Since the P3 microphysics scheme in SCREAM does not partition frozen hydrometeors into separate categories, the histogram in Figure 4.9e is actually for frozen water rather than cloud ice alone as it is in the other models. However, because cold point-overshooting tops are rare compared to RACP cirrus near the cold point, we do not expect the larger sized ice categories to significantly affect the overall distribution.

In the observations as well as the models, there is a consistent decrease in cloud ice with height, but the amounts of cirrus at each level vary greatly between models and observations

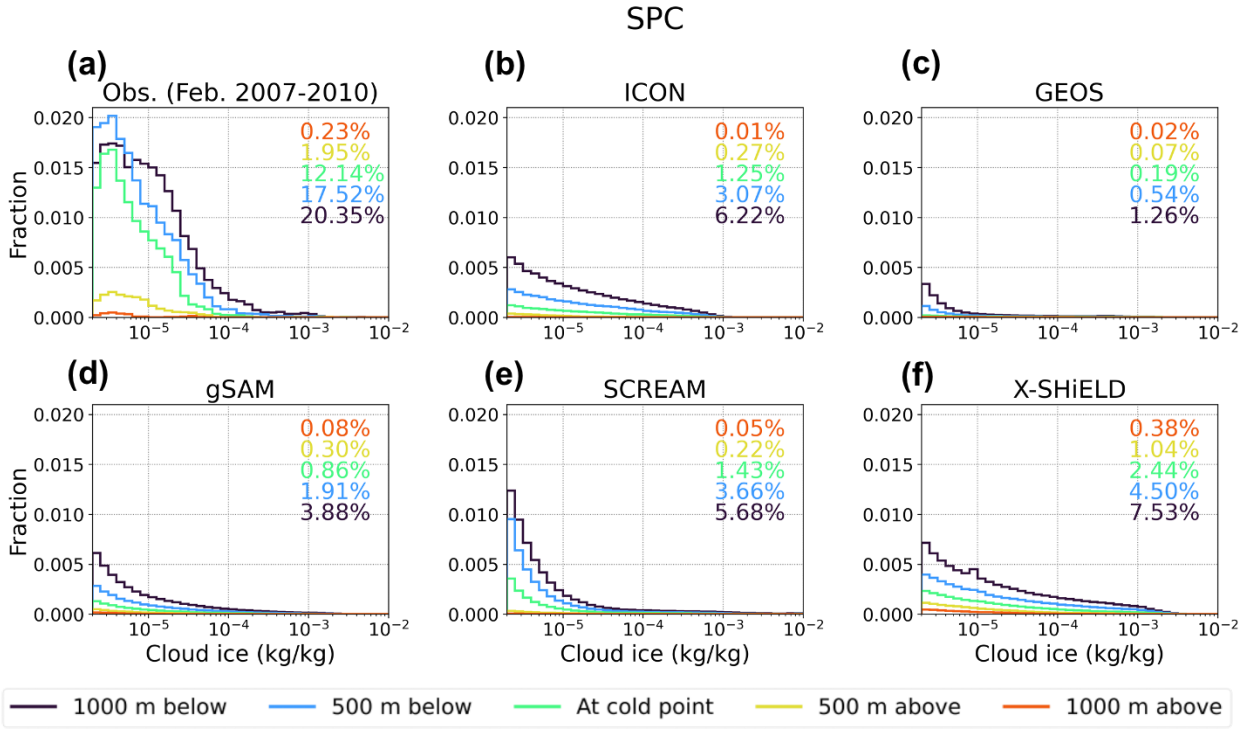

Figure 4.9: Histograms of cloud ice above the radiatively active threshold (2×10^{-6} kg/kg) at levels relative to the cold point for (a) DARDAR observations and (b) ICON, (c) SCREAM, (d) GEOS, (e) gSAM, and (f) X-SHiELD GSRMs in the $10° \times 10°$ SPC region. The numbers in the figure give the cloud fraction of radiatively active cold point cirrus at each z_{cp}-relative level.

(Figure 4.9). RACP cirrus are greatly underestimated in the GSRMs at all levels. The only exception is at $z_{cp} + 1000$ m in X-SHiELD, which simulates RACP cirrus slightly too often. Otherwise, the RACP cirrus fractions in the GSRMs (numbers on each panel of Figure 4.9) are ∼3–20 times less than in the observations at each level. X-SHiELD and SCREAM are closest to the DARDAR observations, but still underestimate the frequency of RACP cirrus by a factor of ∼3–4.

Over land in the AMZ (Figure 4.10), the cirrus frequencies in the models and observations still consistently decrease from $z_{cp} - 1000$ m to $z_{cp} + 1000$ m, but are generally less than half as much as over the ocean in the SPC (Figure 4.9). GEOS (Figure 4.10c) is the exception,

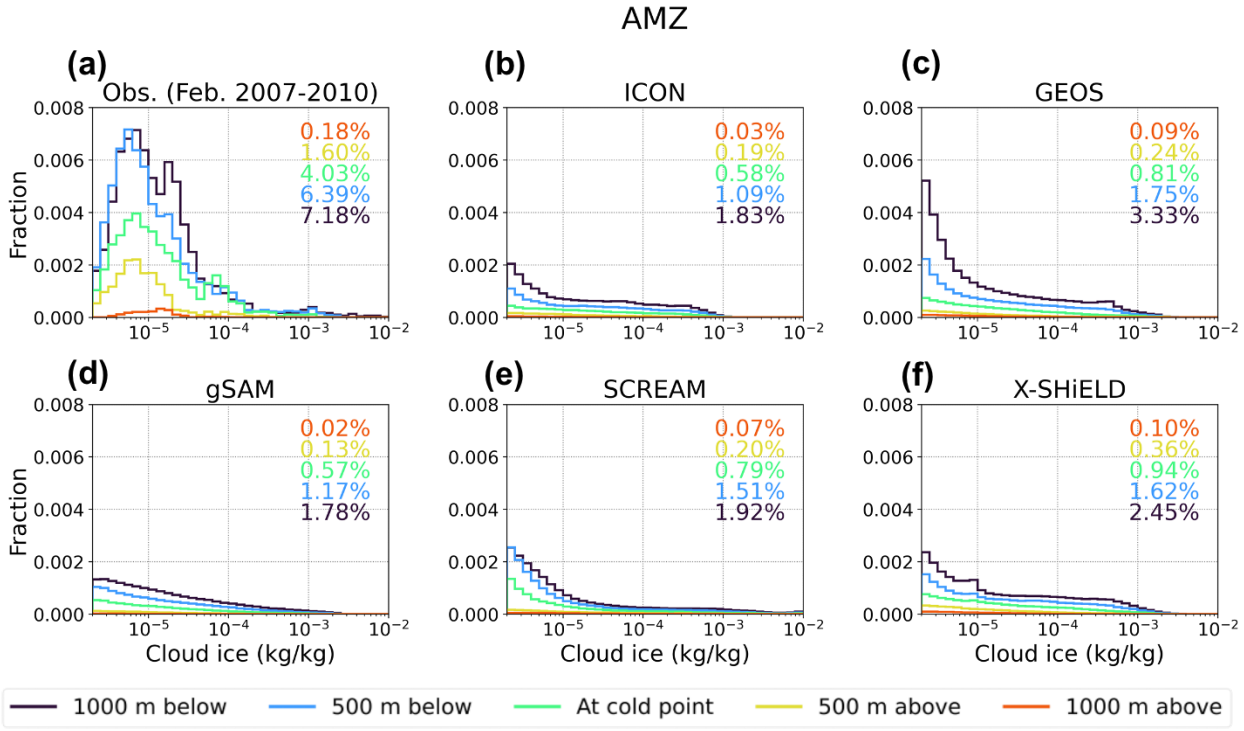

Figure 4.10: As in Figure 4.9, but for the AMZ. Note the different y-axis limits from Figure 4.9.

with cirrus fractions 3–4 times greater over land at all levels. In the observations in the AMZ (Figure 4.10a), there are secondary peaks in the histogram around 2×10^{-5} kg/kg at $z_{cp} - 1000$ m and $z_{cp} - 500$ m and around 7×10^{-5} kg/kg at z_{cp}. These secondary peaks are not present in any of the GSRM distributions. However, in all but gSAM, the frequency distributions become flatter at higher ice water mixing ratios. The secondary peaks in the observed distribution and the ice at 1×10^{-5} kg/kg to $\sim5\times10^{-4}$ kg/kg in the models are likely due to deep convection that reaches up to the cold point or thicker convectively detrained anvils. In the GSRMs, deep convection may be deeper than in the observations and penetrate further past the cold point, resulting in higher ice concentrations near the cold point.

We expect these results to be robust to the choice of parameters used to set the RACP cirrus threshold in Section 4.5.1. Changes in the assumptions that led to the 2×10^{-6} kg/kg

threshold, such as the environmental lapse rate, would change the minimum cloud ice concentration needed for the idealized cirrus cloud to loft. However, adjusting the threshold in either direction to make more or less RACP cirrus still would not make up for the differences between the GSRMs and observations.

4.5.3 Distribution of Radiatively Active Cold Point Cirrus

In Figure 4.11, we replicate the map of $5^\circ \times 5^\circ$ cold point overshoot frequencies in Figure 4.8 for RACP cirrus frequencies at z_{cp} (i.e., $q_i > 2 \times 10^{-6}$ kg/kg). As explained in Section 4.5.1, these cirrus should be capable of lofting above the cold point if the underlying column is cloud-free. The RACP cirrus located at the cold point level are of particular interest because they have the greatest potential to loft the cold point in the following time step. We again calculate the frequencies in each $5^\circ \times 5^\circ$ box by dividing the total number of instances of RACP cirrus at z_{cp} by the total number of columns in space and time. As in Figures 4.9–4.10, we compare the GSRMs to DARDAR observations from February 2007–2010. Overshooting convection occurs so infrequently (Figure 4.8) compared to cirrus that imposing an upper limit on the RACP cirrus definition to exclude overshooting tops does not make a noticeable difference in the overall cirrus frequencies.

For the GSRMs and observations, the areas of frequent RACP cirrus (Figure 4.11) tend to correspond well to the locations of frequent cold point-overshooting convection (Figure 4.8), consistent with the observed collocation of cirrus with deep convection in past studies (e.g., Lee et al., 2009; Sassen et al., 2009; Virts & Houze, 2015). In the observations (Figure 4.11a), there are frequent RACP cirrus over both land and ocean regions, with the highest occurrence over the Pacific warm pool.

The GSRMs simulate similar amounts of RACP cirrus at z_{cp} (Figure 4.11b–f), but vastly underestimate the amount that are detected by DARDAR. If the radiative lofting of cirrus has a significant impact on the cold point, we would expect to see systematically lower and warmer cold points in the GSRMs since they do not produce enough cirrus that should be capable of radiative lofting. Based on Figure 4.3, this is clearly not the case. Therefore,

there is little evidence that the radiative lofting of cirrus clouds near the cold point strongly affects the cold point temperature or height.

As explained in Section 4.5.2, we expect these results to be robust to the choice of minimum ice concentration for RACP cirrus. Adjusting the cloud ice threshold in either direction would not make the models simulate an appropriate amount of RACP cirrus compared to the observations.

4.6 Discussion

In this section, we relate the mean cold point (Figure 4.3), cold point-overshooting convection (Figure 4.8), and the lofting of RACP cirrus (Figure 4.11) to assess the importance of the two mechanisms in determining the cold point temperature and height. Comparing these three figures between models and between different regions in the same model reveals patterns in the relationships with the cold point temperature and height that are consistent in many of the GSRMs, despite differences in how the they simulate cirrus and cold point overshoots.

Cold point overshoots are strongly related to the cold point height and temperature in the GSRMs and observations. This may indicate that the cold point-overshooting tops penetrate into the lower stratosphere and cool the surrounding air, leading to a colder and higher cold point. As noted by Gettelman et al. (2002), however, colder cold points may also allow convection to overshoot more often by destabilizing the upper troposphere. The relationship between cold point overshooting convection and the cold point itself may therefore work both ways; i.e., overshoots cool and raise the cold point, and the colder cold points in turn make it easier for overshoots to occur.

Because the drastic difference in RACP cirrus frequency between the observations and GSRMs is not reflected in either the cold point height or temperature, there is little evidence that the radiative lofting of cirrus significantly affects the mean cold point. Any influence that the RACP cirrus have on the cold point is likely small or short-lived. Still, the collocation between areas of frequent cold point overshoots and frequent RACP cirrus suggests that the cold point overshoots help to form RACP cirrus, either directly through anvil detrainment

or gravity wave temperature perturbations or indirectly by moistening the UTLS. We also expect that some of the RACP cirrus remain above the cold point after lofting as the "other stratospheric cirrus" identified in Section 4.4.1.

The differences in cold point overshoots and RACP cirrus between GSRMs and observations are not sufficient to explain the differences in the mean cold points (Figure 4.3). Other processes aside from cold point-overshooting convection and radiative lofting must also play a key role in setting the cold point, such as the Quasi-Biennial Oscillation and vertical disturbances from waves in the lower stratosphere. These processes occur on much longer timescales than the 40-day period of the DYAMOND2 runs and thus cannot be evaluated here. Still, the strong association between cold point overshoots and colder and higher cold points suggests that cold point-overshooting convection is important for setting the cold point tropopause.

4.7 Summary and Conclusions

In this study, we compare two mechanisms for altering the temperature and height of the tropical cold point tropopause: cold point-overshooting convection and the radiative lofting of cirrus clouds near the cold point. We use GSRMs and satellite observations during a 30-day period in boreal winter. We find that the models reproduce the observed geographic distribution in cold point-overshooting convection well. The GSRMs do not simulate enough cirrus compared to observations, including both thin cirrus above the cold point and RACP cirrus located at the cold point. Our results suggest that the cold point-overshooting convection has a non-negligible influence on the mean cold point temperature and height, acting to cool and lift the cold point. In contrast, cirrus lofting does not significantly affect the mean cold point temperature or height.

One major limitation of our study is the short time period of the DYAMOND2 intercomparison. In models, the stratosphere can take up to six months to reach radiative equilibrium. Other stratospheric processes influencing the cold point also occur on much longer time scales, such as the Quasi-Biennial Oscillation (Tegtmeier et al., 2020b; Sweeney

et al., 2023). Longer GSRM simulations like the recent yearlong X-SHiELD runs (Cheng et al., 2022; Harris et al., 2023) are needed to untangle which processes are most important for determining the cold point temperature and height.

Nevertheless, we find that the DYAMOND2 GSRMs reproduce observed cold point overshoots and radiatively cirrus well enough to study the cold point, providing an important starting point for better understanding the mechanisms controlling the cold point temperature and height in the real atmosphere. Further improvements in the model dynamics controlling vertical velocity and microphysics schemes are needed to better represent the amount of overshooting convection over oceans and cirrus near the cold point. Future studies using longer GSRM simulations would help further advance our understanding of the processes controlling the tropical cold point.

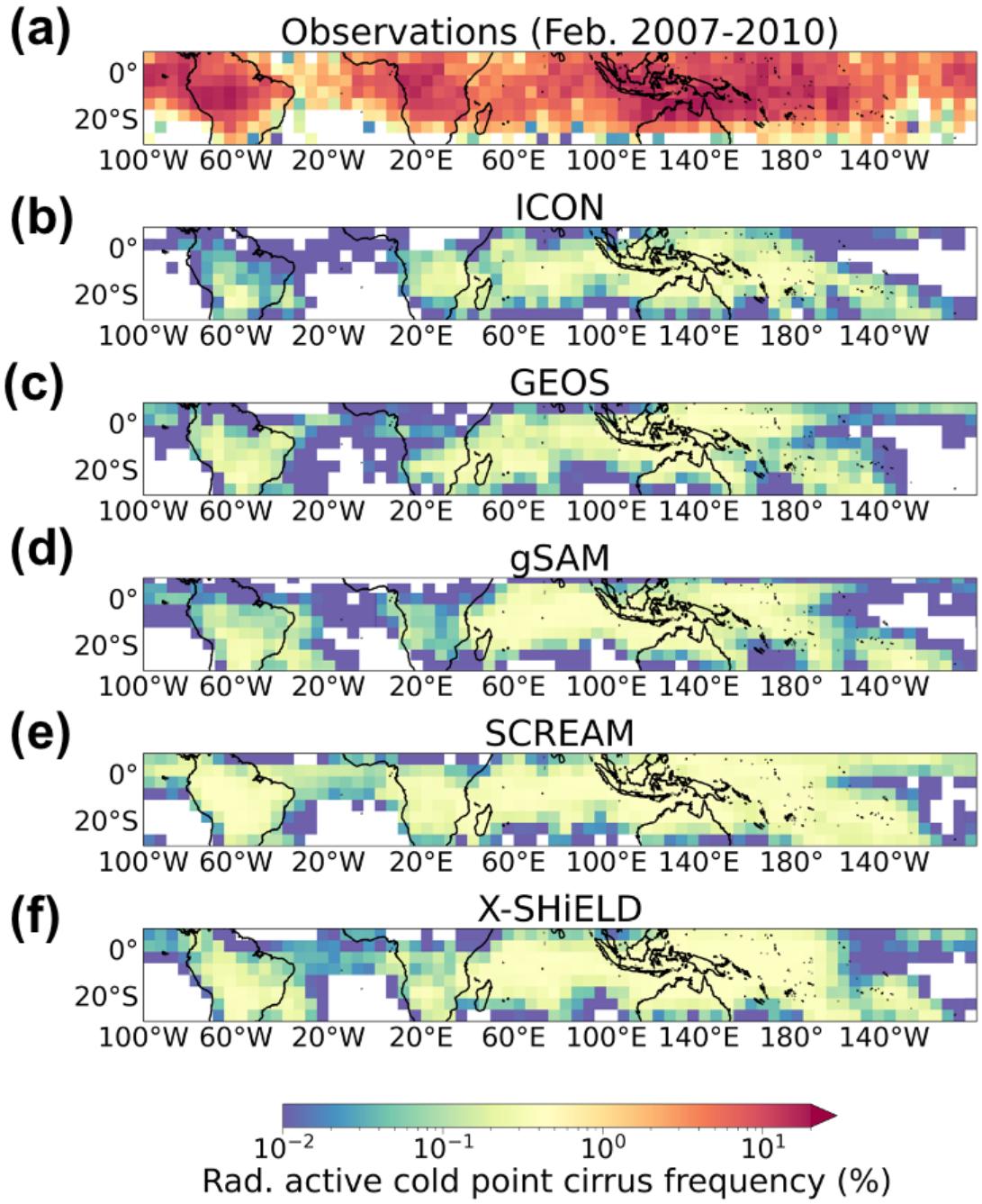

Figure 4.11: Frequency of radiatively active cold point cirrus in the 30-day period within $5° \times 5°$ latitude-longitude boxes for (a) DARDAR observations and (b) ICON, (c) GEOS, (d) gSAM, (e) SCREAM, and (f) X-SHiELD GSRMs. All DARDAR retrievals for February 2007–2010 have been included.

Chapter 5

CONCLUSIONS

In Chapter 2, I identified convection that overshoots the cold point in reanalysis and satellite observations using a radar-calibrated brightness temperature proxy. I found that when the brightness temperature is less than the cold point temperature ($T_b < T_{cp}$), radar-detectable cloud ice is likely to be observed at 500 m above the cold point (z_{cp} + 500 m), indicating cold point-overshooting convection. Calibrating the proxy with radar-detectable ice (and later in Chapter 4, with high frozen water mixing ratios in the GSRMs) helps ensure that the $T_b < T_{cp}$ proxy identifies convection that actually penetrates the cold point tropopause. This choice of variables for this proxy means it can be readily adapted to work with commonly available GSRM output for comparisons to the observations. Here, we focused on the land-ocean contrast in cold point-overshooting convection and cirrus near the cold point and found that cold point overshoots occur more often over land than oceans, but only by ∼30–40%, and that cirrus above the cold point that are not directly related to convection are much more common in the tropics.

GSRMs are promising tools to study overshooting convection. The explicit deep convection and fine (<5 km) horizontal grid spacing should enable them to reproduce individual convective overshoots that cannot be resolved by coarser global climate models with deep convective parameterizations. In Chapter 3, I evaluated the fidelity of a subset of the DYAMOND2 GSRMs in simulating deep convection through an analysis of the precipitation and outgoing longwave radiation. Consistent with findings from my past work with the DYAMOND1 models (Nugent et al., 2022), the DYAMOND2 GSRMs simulate the overall character of deep convection reasonably well but have some notable differences, particularly in how they simulate the contrast between land and ocean convection. Some aspects of the

observed differences in land and ocean deep convection are reproduced by the GSRMs. For example, the GSRMs generally simulate correct timing of the diurnal cycle of convection, where convection has a strong diurnal peak during the afternoon over land but a less pronounced diurnal cycle that peaks in the early morning over oceans (e.g., Yang & Slingo, 2001; Nesbitt & Zipser, 2003; Liu & Zipser, 2008). However, some DYAMOND2 GSRMs produce convection that overshoots the cold point about as often over land as over oceans (see Chapter 4), meaning that simulated cold point overshoots occur too frequently over the oceans in some models. This enhancement suggests that convective updrafts in certain GSRMs are likely too vigorous over ocean regions compared to land. Still, the overall geographic distribution of cold point overshoots is quite consistent between the GSRMs and the observations.

Despite the important inter-model and model/observation differences in cold point overshoots and cirrus, we can still use the DYAMOND2 GSRMs to gain insight into processes in the real atmosphere. In Chapter 4, I used a subset of the DYAMOND2 GSRMs to evaluate whether entrainment from cold point-overshooting convection or the radiative lofting of cirrus near the cold point seems to play a stronger role in setting the temperature and height of the background cold point tropopause. Areas with more frequent cold point overshoots were associated with cooler and higher mean cold points. Radiatively active cold point cirrus tended to occur in areas of frequent overshoots, suggesting that cold point overshoots may help to form these cirrus, but there was little evidence that radiative cirrus lofting significantly influences the mean cold point. In fact, the GSRMs did not simulate enough cirrus overall compared to the DARDAR observations. The GSRMs therefore likely struggle with producing the vertical velocities in the UTLS needed to maintain cirrus layers or with the nucleation in their microphysics schemes that should produce cirrus at and above the cold point.

GSRMs are an important contribution to the hierarchy of climate models and, especially with future improvements, have the potential to help fill some of the gaps in space and time from remote sensing and in situ instruments. GSRMs offer a picture into the global

atmosphere at a high horizontal resolution throughout the day. While observations are more reliable, they can be limited in time (e.g., twice-daily retrievals from sun-synchronous satellites or the timing of a field campaign) or space (e.g., the locations of flight trajectories or stations of ground-based instruments). More work needs to be done to determine which aspects of the model physics and dynamics are most responsible for the differences between simulated and observed deep convection and cirrus so that the potential for GSRMs can be fully realized. Nevertheless, the work presented in this dissertation shows that GSRMs can provide insight into overshooting convection and the cold point tropopause when they are compared to observations.

The next steps of this work would be to compare yearlong and perturbed-climate GSRM simulations to observations. A longer time period would allow for a closer examination of the stratospheric processes that also contribute to the cold point temperature and height but occur on times scales longer than the 30-day DYAMOND period. Additional studies using models with even finer resolutions, such as large-eddy simulations, would help to better understand the small-scale mechanisms (e.g., entrainment) through which cold point overshoots and cirrus lofting can potentially impact the cold point. Perturbed climate simulations, such as those with +4 K sea surface temperatures or quadrupling of atmospheric CO_2, would provide insight into how the relationship between overshooting convection, cirrus, and the cold point may change in a future warmed climate.

Appendix A

SUPPORTING INFORMATION FOR CHAPTER 2

This appendix contains the specific coordinates for each region as well as maps of the time-mean cold point temperatures and heights not shown in Chapter 2. Also included are analogous versions of Figures 2.1–2.3 (Figures A.2–A.4, respectively) for the other regions.

Table A.1: Coordinates of Each Analysis Region

Region Name	Abbreviation	Coordinates
Amazonia	AMZ	47°W–72°W, 30°S–0°
Southern Indian Ocean	IOS	50°E–100°E, 15°S–0°
South Pacific Convergence Zone	SPC	165°E–145°W, 20°S–5°S
Africa	AFR	7°W–35°E, 0°–18°N
Equatorial Indian Ocean	IOE	53°E–95°E, 12°S–6°N
West Pacific	WPC	130°E–180°E, 0°–15°N
East-Central Pacific	ECP	150°W–100°W, 0°–15°N

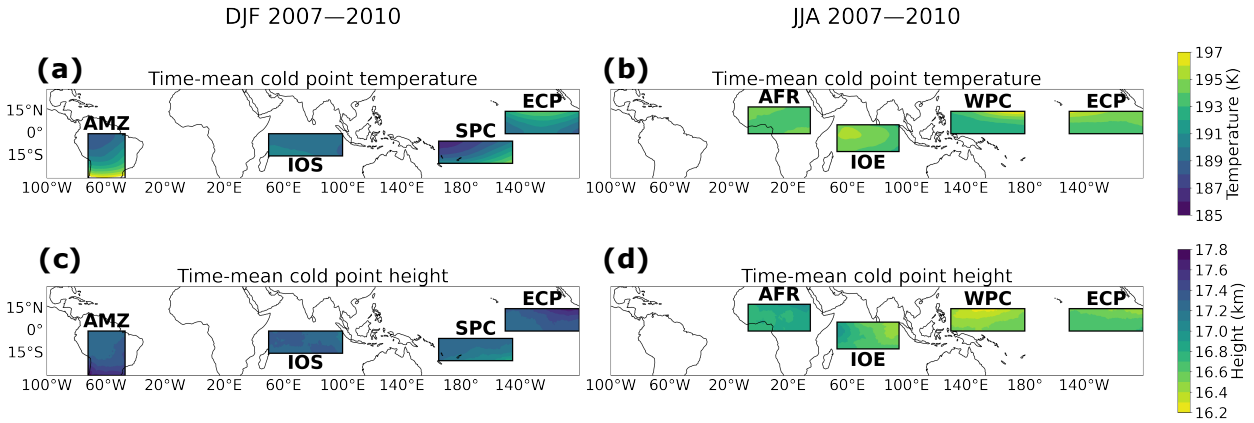

Figure A.1: Time-mean cold point (a)–(b) temperature and (c)–(d) height for (left) DJF and (right) JJA in each analysis region. The color map for height is reversed so that the lowest heights are the same color as the warmest temperatures and vice versa.

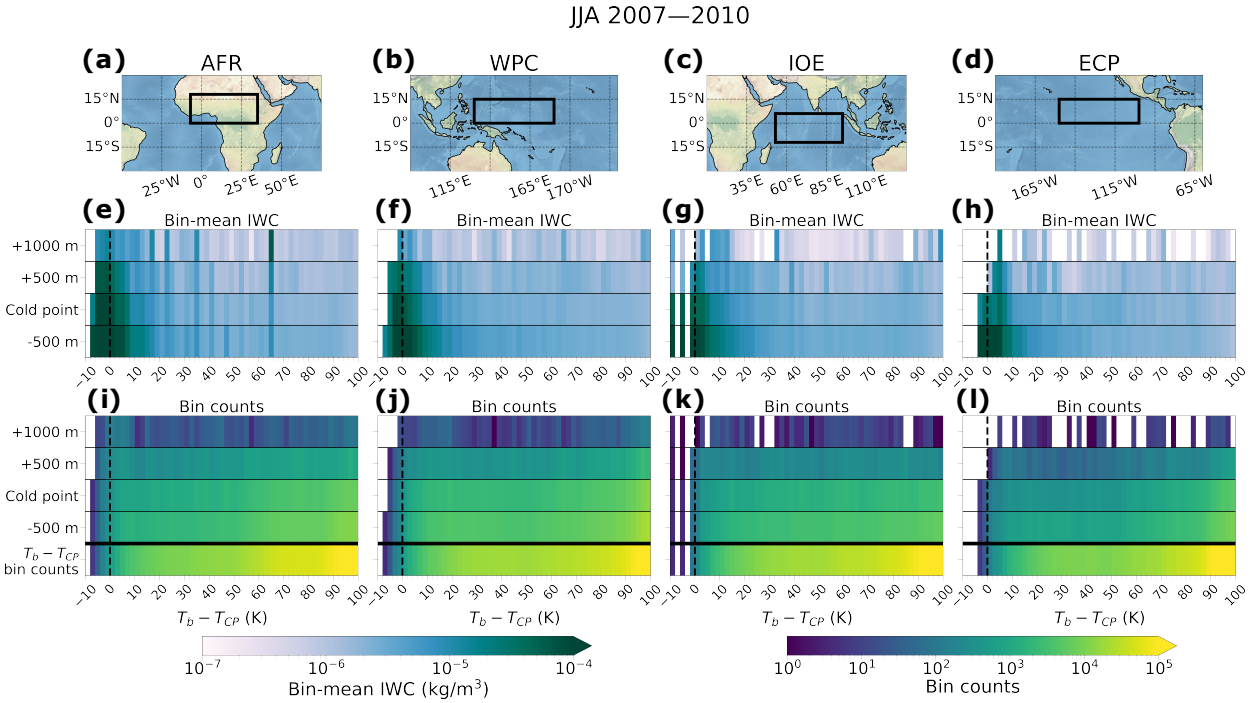

Figure A.2: As in Figure 2.1, but for JJA: Cold point-relative cloud ice binned by $T_b - T_{CP}$ for all DARDAR pixels in JJA 2007–2010. (a)–(d) Maps of each analysis region; (e)–(h) bin-mean IWC at 500 m below to 1000 m above the cold point height; and (i)–(l) bin counts conditioned on when DARDAR detects ice at each cold point-relative level. The row below the thick black line in (i)–(l) shows the total brightness temperature bin counts. The dashed lines in (e)–(l) mark where the brightness temperature equals the cold point. The bin width is 2 K.

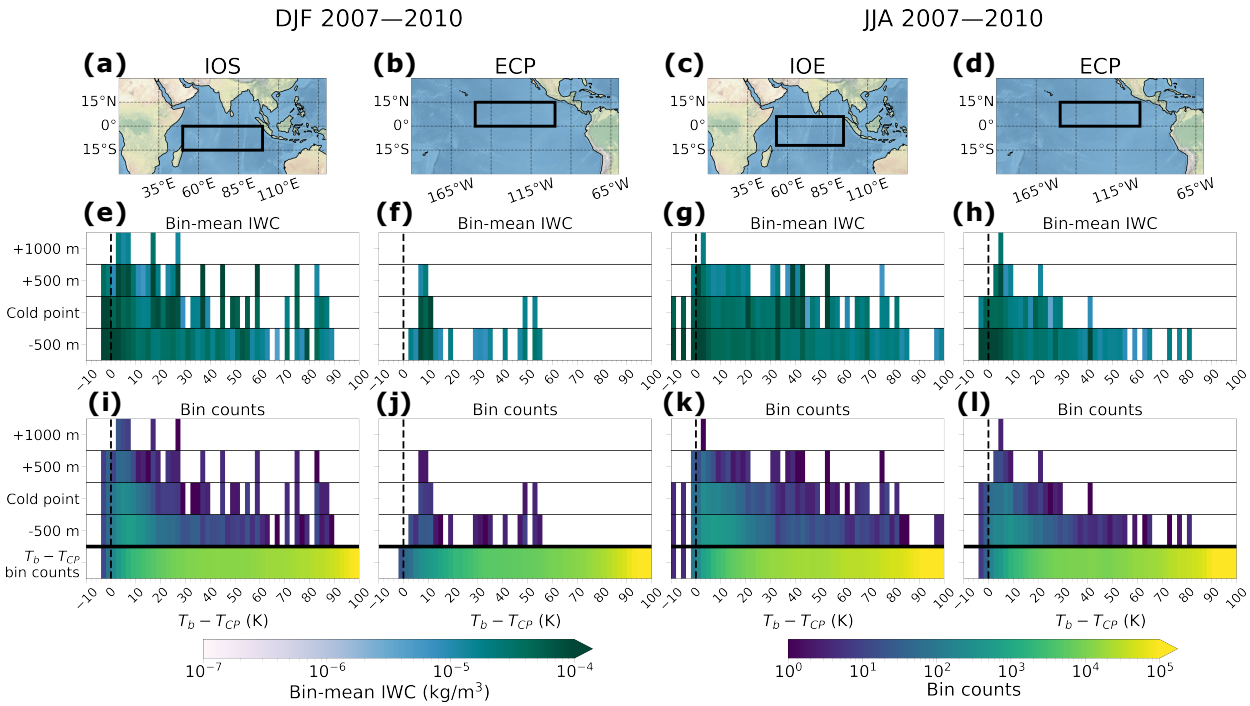

Figure A.3: As in Figure A.2, but restricted to pixels in which the radar and lidar both detect ice; only the regions not included in Figure 3.2 are shown.

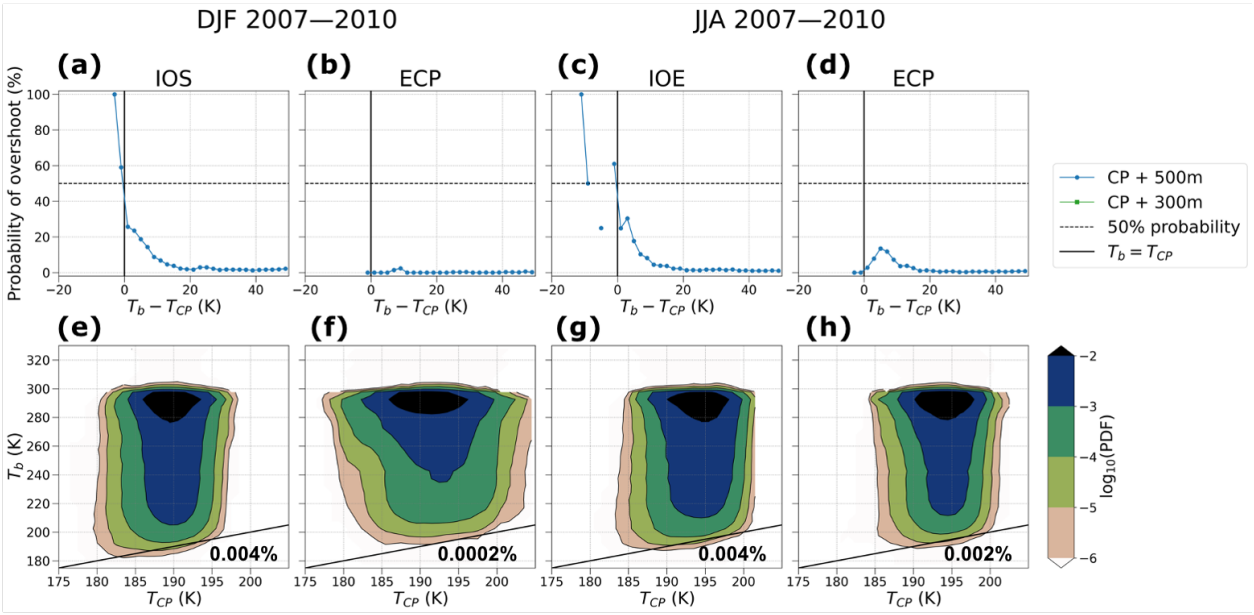

Figure A.4: As in Figure 2.3 but for the other regions in DJF and JJA: (a)–(d) Conditional probability of cold point overshoots (ice at 500 m above the cold point) as a function of $T_b - T_{CP}$. The dashed line indicates a 50% chance of cold point overshoots. (e)–(h) Joint brightness temperature-cold point histograms for all GPM_MERGIR data points. The numbers on the bottom row of plots give the fraction of columns with $T_b < T_{cp}$. In all panels, the solid lines mark where the brightness temperature equals the cold point.

Appendix B

SUPPORTING INFORMATION FOR CHAPTER 4

This appendix contains additional figures for the $10° \times 10°$ regions not shown in Chapter 4. The following figures (B.1 and B.2) are analogous to Figures 4.4 and 4.5, respectively.

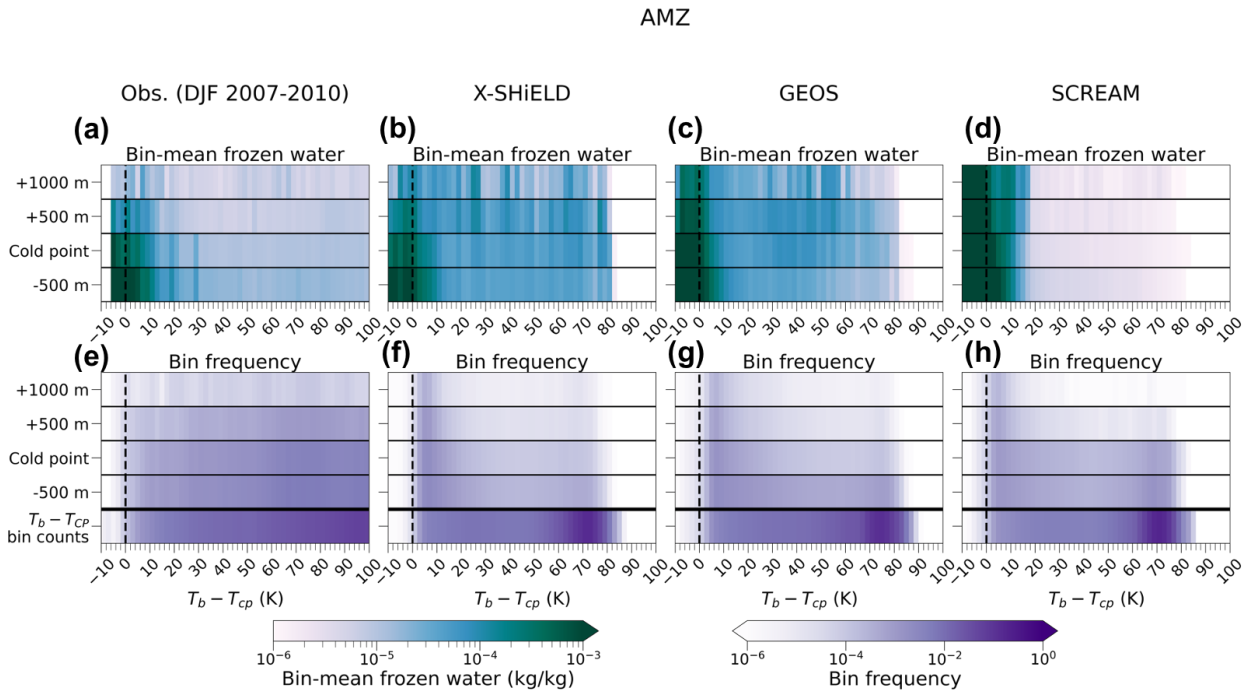

Figure B.1: As in Figure 4.4, but for the AMZ: Cold point-relative frozen water binned by $T_b - T_{cp}$ in the SPC region for (a) observations, (b) X-SHiELD, (c) GEOS, and (d) SCREAM. The top row of plots shows the bin-mean frozen water mixing ratio at 500 m below to 1000 m above the local cold point height. The bottom row of plots shows the bin counts conditioned on when (a) DARDAR detects ice or (b)–(d) the GSRM frozen water exceeds a lower threshold of 1×10^{-6} kg/kg. The total brightness temperature bin counts are shown below the thick black line in the bottom row of plots. The dashed lines mark where the brightness temperature equals the cold point temperature. The bin width is 2 K.

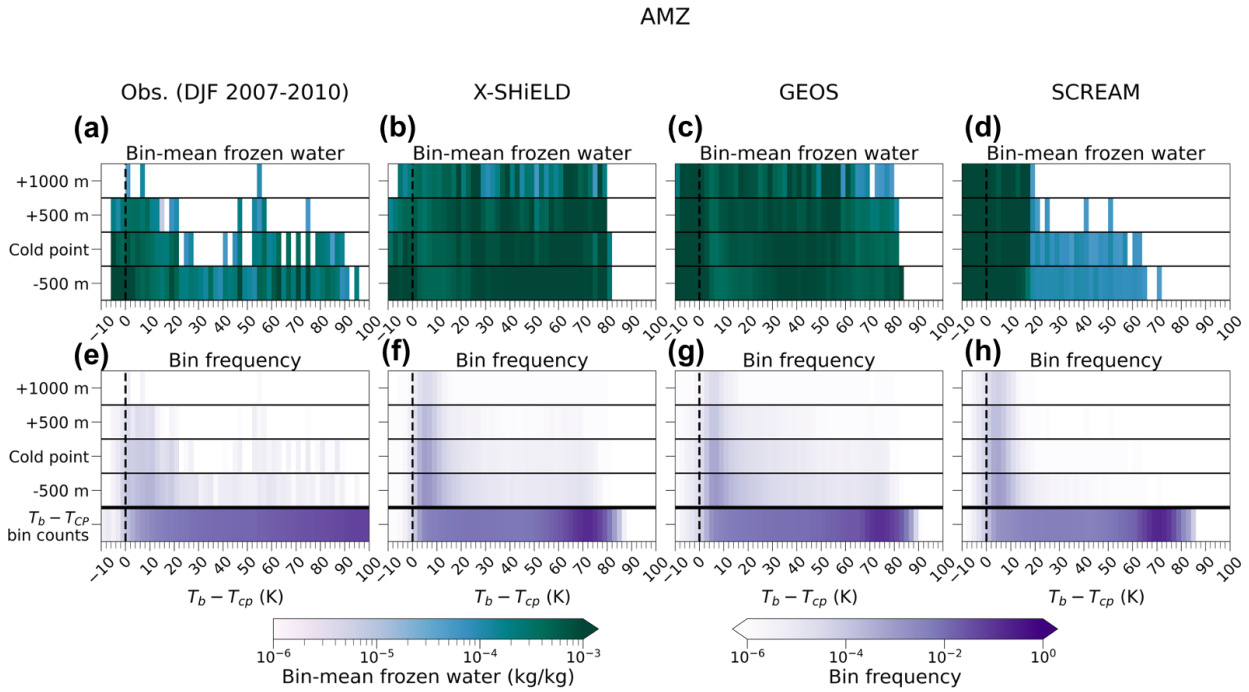

Figure B.2: As in Figure B.1, but restricted to (a) DARDAR pixels detected by both the radar and lidar or (b)–(d) GSRM grid points where the mixing ratio at that level exceeds 5×10^{-5} kg/kg.

BIBLIOGRAPHY

Ali, S., Mehta, S. K., Annamalai, V., Ananthavel, A., & Reddy, R. (2020). Qualitative observations of the cirrus clouds effect on the thermal structure of the tropical tropopause. *Journal of Atmospheric and Solar-Terrestrial Physics*, *211*, 105440. doi: 10.1016/j.jastp.2020.105440

Aumann, H. H., Behrangi, A., & Wang, Y. (2018). Increased Frequency of Extreme Tropical Deep Convection: AIRS Observations and Climate Model Predictions. *Geophysical Research Letters*, *45*(24). doi: 10.1029/2018GL079423

Avery, M. A., Davis, S. M., Rosenlof, K. H., Ye, H., & Dessler, A. E. (2017). Large anomalies in lower stratospheric water vapour and ice during the 2015–2016 El Niño. *Nature Geoscience*, *10*(6), 405–409. doi: 10.1038/ngeo2961

Bechtold, P., Chaboureau, J.-P., Beljaars, A., Betts, A., Köhler, M., Miller, M., & Redelsperger, J.-L. (2004). The simulation of the diurnal cycle of convective precipitation over land in a global model. *Quarterly Journal of the Royal Meteorological Society*, *130*(604), 3119–3137. doi: 10.1256/qj.03.103

Brewer, A. W. (1949). Evidence for a world circulation provided by the measurements of helium and water vapour distribution in the stratosphere. *Quarterly Journal of the Royal Meteorological Society*, *75*(326), 351–363. doi: 10.1002/qj.49707532603

Bucci, S., Legras, B., Sellitto, P., D'Amato, F., Viciani, S., Montori, A., ... Stroh, F. (2020). Deep-convective influence on the upper troposphere–lower stratosphere composition in the Asian monsoon anticyclone region: 2017 StratoClim campaign results. *Atmospheric Chemistry and Physics*, *20*(20), 12193–12210. doi: 10.5194/acp-20-12193-2020

Caldwell, P. M., Terai, C. R., Hillman, B., Keen, N. D., Bogenschutz, P., Lin, W., ... Zender, C. S. (2021). Convection-Permitting Simulations With the E3SM Global

Atmosphere Model. *Journal of Advances in Modeling Earth Systems*, *13*(11). doi: 10.1029/2021MS002544

Cazenave, Q., Ceccaldi, M., Delanoë, J., Pelon, J., Groß, S., & Heymsfield, A. (2019). Evolution of DARDAR-CLOUD ice cloud retrievals: new parameters and impacts on the retrieved microphysical properties. *Atmospheric Measurement Techniques*, *12*(5), 2819–2835. doi: 10.5194/amt-12-2819-2019

Chae, J. H., Wu, D. L., Read, W. G., & Sherwood, S. C. (2011). The role of tropical deep convective clouds on temperature, water vapor, and dehydration in the tropical tropopause layer (TTL). *Atmospheric Chemistry and Physics*, *11*(8), 3811–3821. doi: 10.5194/acp-11-3811-2011

Chang, K.-W., & L'Ecuyer, T. (2020). Influence of gravity wave temperature anomalies and their vertical gradients on cirrus clouds in the tropical tropopause layer – a satellite-based view. *Atmospheric Chemistry and Physics*, *20*(21), 12499–12514. doi: 10.5194/acp-20-12499-2020

Cheng, K.-Y., Harris, L., Bretherton, C., Merlis, T. M., Bolot, M., Zhou, L., ... Fueglistaler, S. (2022). Impact of Warmer Sea Surface Temperature on the Global Pattern of Intense Convection: Insights From a Global Storm Resolving Model. *Geophysical Research Letters*, *49*(16), e2022GL099796. doi: 10.1029/2022GL099796

Corti, T., Luo, B. P., de Reus, M., Brunner, D., Cairo, F., Mahoney, M. J., ... Peter, T. (2008). Unprecedented evidence for deep convection hydrating the tropical stratosphere: CONVECTIVE HYDRATION. *Geophysical Research Letters*, *35*(10). doi: 10.1029/2008GL033641

Corti, T., Luo, B. P., Fu, Q., Vomel, H., & Peter, T. (2006). The impact of cirrus clouds on tropical troposphere-to-stratosphere transport. *Atmos. Chem. Phys.*, 9.

Dauhut, T., & Hohenegger, C. (2022). The Contribution of Convection to the Stratospheric Water Vapor: The First Budget Using a Global Storm-Resolving Model. *Journal of Geophysical Research: Atmospheres*, *127*(5). doi: 10.1029/2021JD036295

Delanoë, J. (2023). *DARDAR CLOUD - Heymfield's composite mass-size relationship.*

DARDAR-CLOUD v3.10. Accessed 2023-02-01. Aeris. (Dataset) doi: doi.org/10.25326/449

Delanoë, J., & Hogan, R. J. (2008). A variational scheme for retrieving ice cloud properties from combined radar, lidar, and infrared radiometer. *Journal of Geophysical Research*, *113*(D7), D07204. doi: 10.1029/2007JD009000

Delanoë, J., & Hogan, R. J. (2010). Combined CloudSat-CALIPSO-MODIS retrievals of the properties of ice clouds. *Journal of Geophysical Research*, *115*, D00H29. doi: 10.1029/2009JD012346

Dessler, A. E. (2002). The effect of deep, tropical convection on the tropical tropopause layer. *Journal of Geophysical Research*, *107*(D3), 4033. doi: 10.1029/2001JD000511

Dessler, A. E., Ye, H., Wang, T., Schoeberl, M., Oman, L., Douglass, A., ... Portmann, R. (2016). Transport of ice into the stratosphere and the humidification of the stratosphere over the 21st century. *Geophysical Research Letters*, *43*(5), 2323–2329. doi: 10.1002/2016GL067991

Dinh, T. P., Durran, D. R., & Ackerman, T. P. (2010). Maintenance of tropical tropopause layer cirrus. *Journal of Geophysical Research: Atmospheres*, *115*(D2). doi: 10.1029/2009JD012735

Dion, I.-A., Ricaud, P., Haynes, P., Carminati, F., & Dauhut, T. (2019). Ice injected into the tropopause by deep convection – Part 1: In the austral convective tropics. *Atmospheric Chemistry and Physics*, *19*(9), 6459–6479. doi: 10.5194/acp-19-6459-2019

Doelling, D. R., Sun, M., Nguyen, L. T., Nordeen, M. L., Haney, C. O., Keyes, D. F., & Mlynczak, P. E. (2016). Advances in Geostationary-Derived Longwave Fluxes for the CERES Synoptic (SYN1deg) Product. *Journal of Atmospheric and Oceanic Technology*, *33*(3), 503–521. doi: 10.1175/JTECH-D-15-0147.1

Duda, J. D., & Gallus, W. A. (2013). The Impact of Large-Scale Forcing on Skill of Simulated Convective Initiation and Upscale Evolution with Convection-Allowing Grid Spacings in the WRF*. *Weather and Forecasting*, *28*(4), 994–1018. doi: 10.1175/WAF-D-13-00005.1

Duras, J., Ziemen, F., & Klocke, D. (2021, March). *The DYAMOND Winter data collection* (Tech. Rep. No. EGU21-4687). Copernicus Meetings. Retrieved 2023-07-17, from `https://meetingorganizer.copernicus.org/EGU21/EGU21-4687.html` (Conference Name: EGU21) doi: 10.5194/egusphere-egu21-4687

Durran, D. R., Dinh, T., Ammerman, M., & Ackerman, T. (2009). The Mesoscale Dynamics of Thin Tropical Tropopause Cirrus. *Journal of the Atmospheric Sciences*, *66*(9), 2859–2873. doi: 10.1175/2009JAS3046.1

Fueglistaler, S., Dessler, A. E., Dunkerton, T. J., Folkins, I., Fu, Q., & Mote, P. W. (2009). Tropical tropopause layer. *Reviews of Geophysics*, *47*(1). doi: 10.1029/2008RG000267

Gettelman, A., Salby, M. L., & Sassi, F. (2002). Distribution and influence of convection in the tropical tropopause region: CONVECTION IN THE TROPOPAUSE REGION. *Journal of Geophysical Research: Atmospheres*, *107*(D10), ACL 6–1–ACL 6–12. doi: 10.1029/2001JD001048

Harris, L., Zhou, L., Kaltenbaugh, A., Clark, S., Cheng, K.-Y., & Bretherton, C. (2023). A Global Survey of Rotating Convective Updrafts in the GFDL X-SHiELD 2021 Global Storm Resolving Model. *Journal of Geophysical Research: Atmospheres*, *128*(10), e2022JD037823. doi: 10.1029/2022JD037823

Harris, L., Zhou, L., Lin, S.-J., Chen, J.-H., Chen, X., Gao, K., ... Stern, W. (2020). GFDL SHiELD: A Unified System for Weather-to-Seasonal Prediction. *Journal of Advances in Modeling Earth Systems*, *12*(10), e2020MS002223. doi: 10.1029/2020MS002223

Hartmann, D. L., Holton, J. R., & Fu, Q. (2001). The heat balance of the tropical tropopause, cirrus, and stratospheric dehydration. *Geophysical Research Letters*, *28*(10), 1969–1972. doi: 10.1029/2000GL012833

Hatsushika, H., & Yamazaki, K. (2001). Interannual variations of temperature and vertical motion at the tropical tropopause associated with ENSO. *Geophysical Research Letters*, *28*(15), 2891–2894. doi: 10.1029/2001GL012977

Hersbach, H., Bell, B., Berrisford, P., Hirahara, S., Horányi, A., Muñoz-Sabater, J., ... Thépaut, J. (2020). The ERA5 global reanalysis. *Quarterly Journal of the Royal*

Meteorological Society, *146*(730), 1999–2049. doi: 10.1002/qj.3803

Hersbach, H., Bell, B., Berrisford, P., Hirahara, S., Horányi, A., Muñoz-Sabater, J., ... Thépaut, J.-N. (2017). *Complete ERA5 from 1940: Fifth generation of ECMWF atmospheric reanalyses of the global climate.* Accessed 2023-02-01. Copernicus Climate Change Service (C3S) Data Store (CDS). (Dataset) doi: 10.24381/cds.143582cf

Highwood, E. J., & Hoskins, B. J. (1998). The tropical tropopause. *Quarterly Journal of the Royal Meteorological Society*, *124*(549), 1579–1604. doi: 10.1002/qj.49712454911

Hoffmann, L., & Spang, R. (2022). An assessment of tropopause characteristics of the ERA5 and ERA-Interim meteorological reanalyses. *Atmospheric Chemistry and Physics*, *22*(6), 4019–4046. doi: 10.5194/acp-22-4019-2022

Holton, J. R., & Gettelman, A. (2001). Horizontal transport and the dehydration of the stratosphere. *Geophysical Research Letters*, *28*(14), 2799–2802. doi: 10.1029/2001GL013148

Hong, G., Heygster, G., Miao, J., & Kunzi, K. (2005). Detection of tropical deep convective clouds from AMSU-B water vapor channels measurements. *Journal of Geophysical Research: Atmospheres*, *110*(D5). doi: 10.1029/2004JD004949

Huffman, G. J., Stocker, E. F., Bolvin, D. T., Nelkin, E. J., & Jackson Tan. (2019). *GPM IMERG Final Precipitation L3 Half Hourly 0.1 degree x 0.1 degree V06, Greenbelt, MD, Goddard Earth Sciences Data and Information Services Center (GES DISC).* Retrieved 2022-04-14, from `https://doi.org/10.5067/GPM/IMERG/3B-HH/06` (Dataset) doi: 10.5067/GPM/IMERG/3B-HH/06

Iwasaki, S., Shibata, T., Nakamoto, J., Okamoto, H., Ishimoto, H., & Kubota, H. (2010). Characteristics of deep convection measured by using the A-train constellation. *Journal of Geophysical Research: Atmospheres*, *115*(D6). doi: 10.1029/2009JD013000

Jain, A. R., Panwar, V., Johny, C. J., Mandal, T. K., Rao, V. R., Gautam, R., & Dhaka, S. K. (2011). Occurrence of extremely low cold point tropopause temperature during summer monsoon season: ARMEX campaign and CHAMP and COSMIC satellite observations. *Journal of Geophysical Research*, *116*(D3), D03102. doi: 10.1029/2010JD014340

Janowiak, J., Joyce, B., & Xie, P. (2017). *NCEP/CPC L3 Half Hourly 4km Global (60S - 60N) Merged IR V1.* Accessed 2023-02-01. (Edited by Andrey Savtchenko, Greenbelt, MD, Goddard Earth Sciences Data and Information Services Center (GES DISC). Dataset) doi: 10.5067/P4HZB9N27EKU

Jensen, E. J., Ackerman, A. S., & Smith, J. A. (2007). Can overshooting convection dehydrate the tropical tropopause layer? *Journal of Geophysical Research*, *112*(D11), D11209. doi: 10.1029/2006JD007943

Jensen, E. J., Toon, O. B., Pfister, L., & Selkirk, H. B. (1996a). Dehydration of the upper troposphere and lower stratosphere by subvisible cirrus clouds near the tropical tropopause. *Geophysical Research Letters*, *23*(8), 825–828. doi: 10.1029/96GL00722

Jensen, E. J., Toon, O. B., Selkirk, H. B., Spinhirne, J. D., & Schoeberl, M. R. (1996b). On the formation and persistence of subvisible cirrus clouds near the tropical tropopause. *Journal of Geophysical Research: Atmospheres*, *101*(D16), 21361–21375. doi: 10.1029/95JD03575

Jensen, E. J., Ueyama, R., Pfister, L., Bui, T. V., Alexander, M. J., Podglajen, A., ... Schoeberl, M. R. (2016). High-frequency gravity waves and homogeneous ice nucleation in tropical tropopause layer cirrus: WAVES AND ICE NUCLEATION. *Geophysical Research Letters*, *43*(12), 6629–6635. doi: 10.1002/2016GL069426

Judt, F., Klocke, D., Rios-Berrios, R., Vanniere, B., Ziemen, F., Auger, L., ... Zhou, L. (2021). Tropical Cyclones in Global Storm-Resolving Models. *Journal of the Meteorological Society of Japan. Ser. II*, *99*(3), 579–602. doi: 10.2151/jmsj.2021-029

Kelley, O. A., Stout, J., Summers, M., & Zipser, E. J. (2010). Do the Tallest Convective Cells over the Tropical Ocean Have Slow Updrafts? *Monthly Weather Review*, *138*(5), 1651–1672. doi: 10.1175/2009MWR3030.1

Khairoutdinov, M. F., Blossey, P. N., & Bretherton, C. S. (2022). Global System for Atmospheric Modeling: Model Description and Preliminary Results. *Journal of Advances in Modeling Earth Systems*, *14*(6), e2021MS002968. doi: 10.1029/2021MS002968

Khaykin, S. M., Moyer, E., Krämer, M., Clouser, B., Bucci, S., Legras, B., ... Stroh,

F. (2022). Persistence of moist plumes from overshooting convection in the Asian monsoon anticyclone. *Atmospheric Chemistry and Physics*, *22*(5), 3169–3189. doi: 10.5194/acp-22-3169-2022

Kim, J., & Son, S.-W. (2012). Tropical Cold-Point Tropopause: Climatology, Seasonal Cycle, and Intraseasonal Variability Derived from COSMIC GPS Radio Occultation Measurements. *Journal of Climate*, *25*(15), 5343–5360. doi: 10.1175/JCLI-D-11-00554.1

Klocke, D., Brueck, M., Hohenegger, C., & Stevens, B. (2017). Rediscovery of the doldrums in storm-resolving simulations over the tropical Atlantic. *Nature Geoscience*, *10*(12), 891–896. doi: 10.1038/s41561-017-0005-4

Krämer, M., Rolf, C., Luebke, A., Afchine, A., Spelten, N., Costa, A., ... Avallone, L. (2016). A microphysics guide to cirrus clouds – Part 1: Cirrus types. *Atmospheric Chemistry and Physics*, *16*(5), 3463–3483. doi: 10.5194/acp-16-3463-2016

Kuang, Z., & Bretherton, C. S. (2004). Convective Influence on the Heat Balance of the Tropical Tropopause Layer: A Cloud-Resolving Model Study. *Journal of the Atmospheric Sciences*, *61*(23), 2919–2927. doi: 10.1175/JAS-3306.1

Lee, J., Yang, P., Dessler, A. E., Gao, B.-C., & Platnick, S. (2009). Distribution and Radiative Forcing of Tropical Thin Cirrus Clouds. *Journal of the Atmospheric Sciences*, *66*(12), 3721–3731. doi: 10.1175/2009JAS3183.1

Li, H., Wei, X., Min, M., Li, B., Nong, Z., & Chen, L. (2022). A Dataset of Overshooting Cloud Top from 12-Year CloudSat/CALIOP Joint Observations. *Remote Sensing*, *14*(10), 2417. doi: 10.3390/rs14102417

Lin, S.-J. (2004). A "Vertically Lagrangian" Finite-Volume Dynamical Core for Global Models. *Monthly Weather Review*, *132*(10), 2293–2307. doi: 10.1175/1520-0493(2004)132⟨2293:AVLFDC⟩2.0.CO;2

Liou, Y.-A., & Ravindra Babu, S. (2020). ENSO signatures observed in tropical tropopause layer parameters using long-term COSMIC RO data. *GPS Solutions*, *24*(4), 98. doi: 10.1007/s10291-020-01009-7

Liu, C., & Zipser, E. J. (2005). Global distribution of convection penetrating the tropical tropopause. *Journal of Geophysical Research*, *110*(D23), D23104. doi: 10.1029/2005JD006063

Liu, C., & Zipser, E. J. (2008). Diurnal cycles of precipitation, clouds, and lightning in the tropics from 9 years of TRMM observations. *Geophysical Research Letters*, *35*(4). doi: 10.1029/2007GL032437

Liu, C., Zipser, E. J., & Nesbitt, S. W. (2007). Global Distribution of Tropical Deep Convection: Different Perspectives from TRMM Infrared and Radar Data. *Journal of Climate*, *20*(3), 489–503. doi: 10.1175/JCLI4023.1

Liu, N., & Liu, C. (2016). Global distribution of deep convection reaching tropopause in 1 year GPM observations. *Journal of Geophysical Research: Atmospheres*, *121*(8), 3824–3842. doi: 10.1002/2015JD024430

Liu, N., Liu, C., & Hayden, L. (2020). Climatology and Detection of Overshooting Convection From 4 Years of GPM Precipitation Radar and Passive Microwave Observations. *Journal of Geophysical Research: Atmospheres*, *125*(7). doi: 10.1029/2019JD032003

Luo, Z., Liu, G. Y., & Stephens, G. L. (2008). CloudSat adding new insight into tropical penetrating convection. *Geophysical Research Letters*, *35*(19), L19819. doi: 10.1029/2008GL035330

Morrison, H., & Milbrandt, J. A. (2015). Parameterization of Cloud Microphysics Based on the Prediction of Bulk Ice Particle Properties. Part I: Scheme Description and Idealized Tests. *Journal of the Atmospheric Sciences*, *72*(1), 287–311. doi: 10.1175/JAS-D-14-0065.1

Munchak, L. A., & Pan, L. L. (2014). Separation of the lapse rate and the cold point tropopauses in the tropics and the resulting impact on cloud top-tropopause relationships. *Journal of Geophysical Research: Atmospheres*, *119*(13), 7963–7978. doi: 10.1002/2013JD021189

Nesbitt, S. W., & Zipser, E. J. (2003). The Diurnal Cycle of Rainfall and Convective Intensity according to Three Years of TRMM Measurements. *JOURNAL OF CLIMATE*, *16*,

20.

Nugent, J. M., & Bretherton, C. S. (2023). Tropical convection overshoots the cold point tropopause nearly as often over warm oceans as over land. Manuscript submitted for publication.

Nugent, J. M., Turbeville, S. M., Bretherton, C. S., Blossey, P. N., & Ackerman, T. P. (2022). Tropical Cirrus in Global Storm-Resolving Models: 1. Role of Deep Convection. *Earth and Space Science*, *9*(2). doi: 10.1029/2021EA001965

Pan, L. L., Honomichl, S. B., Bui, T. V., Thornberry, T., Rollins, A., Hintsa, E., & Jensen, E. J. (2018). Lapse Rate or Cold Point: The Tropical Tropopause Identified by In Situ Trace Gas Measurements. *Geophysical Research Letters*, *45*(19). doi: 10.1029/2018GL079573

Pan, L. L., & Munchak, L. A. (2011). Relationship of cloud top to the tropopause and jet structure from CALIPSO data. *Journal of Geophysical Research: Atmospheres*, *116*(D12). doi: 10.1029/2010JD015462

Pommereau, J.-P. (2010). Troposphere-to-stratosphere transport in the tropics. *Comptes Rendus Geoscience*, *342*(4-5), 331–338. doi: 10.1016/j.crte.2009.10.015

Proud, S. R., & Bachmeier, S. (2021). Record-Low Cloud Temperatures Associated With a Tropical Deep Convective Event. *Geophysical Research Letters*, *48*(6). doi: 10.1029/2020GL092261

Putman, W. M. (2021, March). *Overcoming the challenges of increasing resolution and complexity in GEOS* (Tech. Rep. No. EGU21-12782). Copernicus Meetings. Retrieved 2023-07-17, from `https://meetingorganizer.copernicus.org/EGU21/EGU21-12782.html` (Conference Name: EGU21) doi: 10.5194/egusphere-egu21-12782

Putman, W. M., & Lin, S.-J. (2007). Finite-volume transport on various cubed-sphere grids. *Journal of Computational Physics*, *227*(1), 55–78. doi: 10.1016/j.jcp.2007.07.022

Putman, W. M., & Suarez, M. (2011). Cloud-system resolving simulations with the NASA Goddard Earth Observing System global atmospheric model (GEOS-5). *Geophysical Research Letters*, *38*(16). doi: 10.1029/2011GL048438

Randel, W. J., & Jensen, E. J. (2013). Physical processes in the tropical tropopause layer and their roles in a changing climate. *Nature Geoscience*, *6*(3), 169–176. doi: 10.1038/ngeo1733

Randel, W. J., & Park, M. (2019). Diagnosing Observed Stratospheric Water Vapor Relationships to the Cold Point Tropical Tropopause. *Journal of Geophysical Research: Atmospheres*, *124*(13), 7018–7033. doi: 10.1029/2019JD030648

Randel, W. J., Wu, F., Oltmans, S. J., Rosenlof, K., & Nedoluha, G. E. (2004). Interannual Changes of Stratospheric Water Vapor and Correlations with Tropical Tropopause Temperatures. *Journal of the Atmospheric Sciences*, *61*(17), 2133–2148. doi: 10.1175/1520-0469(2004)061⟨2133:ICOSWV⟩2.0.CO;2

Rossow, W. B., & Pearl, C. (2007). 22-Year survey of tropical convection penetrating into the lower stratosphere. *Geophysical Research Letters*, *34*(4), L04803. doi: 10.1029/2006GL028635

Sassen, K., Wang, Z., & Liu, D. (2009). Cirrus clouds and deep convection in the tropics: Insights from CALIPSO and CloudSat. *Journal of Geophysical Research*, *114*, D00H06. doi: 10.1029/2009JD011916

Seidel, D. J., Ross, R. J., Angell, J. K., & Reid, G. C. (2001). Climatological characteristics of the tropical tropopause as revealed by radiosondes. *Journal of Geophysical Research: Atmospheres*, *106*(D8), 7857–7878. doi: 10.1029/2000JD900837

Solomon, S., Rosenlof, K. H., Portmann, R. W., Daniel, J. S., Davis, S. M., Sanford, T. J., & Plattner, G.-K. (2010). Contributions of Stratospheric Water Vapor to Decadal Changes in the Rate of Global Warming. *Science*, *327*(5970), 1219–1223. doi: 10.1126/science.1182488

Stevens, B., Satoh, M., Auger, L., Biercamp, J., Bretherton, C. S., Chen, X., ... Zhou, L. (2019). DYAMOND: the DYnamics of the Atmospheric general circulation Modeled On Non-hydrostatic Domains. *Progress in Earth and Planetary Science*, *6*(1), 61. doi: 10.1186/s40645-019-0304-z

Suneeth, K. V., Das, S. S., & Das, S. K. (2017). Diurnal variability of the global tropical

tropopause: results inferred from COSMIC observations. *Climate Dynamics*, *49*(9-10), 3277–3292. doi: 10.1007/s00382-016-3512-x

Sweeney, A., Fu, Q., Pahlavan, H. A., & Haynes, P. (2023). Seasonality of the QBO Impact on Equatorial Clouds. *Journal of Geophysical Research: Atmospheres*, *128*(7), e2022JD037737. doi: 10.1029/2022JD037737

Takahashi, H., & Luo, Z. J. (2014). Characterizing tropical overshooting deep convection from joint analysis of CloudSat and geostationary satellite observations: TROPICAL DEEP CONVECTION BY CLOUDSAT. *Journal of Geophysical Research: Atmospheres*, *119*(1), 112–121. doi: 10.1002/2013JD020972

Tegtmeier, S., Anstey, J., Davis, S., Dragani, R., Harada, Y., Ivanciu, I., ... Wright, J. S. (2020a). Temperature and tropopause characteristics from reanalyses data in the tropical tropopause layer. *Atmospheric Chemistry and Physics*, *20*(2), 753–770. doi: 10.5194/acp-20-753-2020

Tegtmeier, S., Anstey, J., Davis, S., Ivanciu, I., Jia, Y., McPhee, D., & Pilch Kedzierski, R. (2020b). Zonal Asymmetry of the QBO Temperature Signal in the Tropical Tropopause Region. *Geophysical Research Letters*, *47*(24), e2020GL089533. doi: 10.1029/2020GL089533

Tian, W., Huang, J., Zhang, J., Xie, F., Wang, W., & Peng, Y. (2023). Role of Stratospheric Processes in Climate Change: Advances and Challenges. *Advances in Atmospheric Sciences*. doi: 10.1007/s00376-023-2341-1

Tseng, H.-H., & Fu, Q. (2017). Tropical tropopause layer cirrus and its relation to tropopause. *Journal of Quantitative Spectroscopy and Radiative Transfer*, *188*, 118–131. doi: 10.1016/j.jqsrt.2016.05.029

Turbeville, S. M., Nugent, J. M., Ackerman, T. P., Bretherton, C. S., & Blossey, P. N. (2022). Tropical Cirrus in Global Storm-Resolving Models: 2. Cirrus Life Cycle and Top-of-Atmosphere Radiative Fluxes. *Earth and Space Science*, *9*(2). doi: 10.1029/2021EA001978

Ueyama, R., Jensen, E. J., & Pfister, L. (2018). Convective Influence on the Humidity

and Clouds in the Tropical Tropopause Layer During Boreal Summer. *Journal of Geophysical Research: Atmospheres*. doi: 10.1029/2018JD028674

Ueyama, R., Schoeberl, M., Jensen, E., Pfister, L., Park, M., & Ryoo, J.-M. (2023). Convective Impact on the Global Lower Stratospheric Water Vapor Budget. *Journal of Geophysical Research: Atmospheres*, *128*(6), e2022JD037135. doi: 10.1029/2022JD037135

Vernier, J.-P., Pommereau, J.-P., Thomason, L. W., Pelon, J., Garnier, A., Deshler, T., ... Nielsen, J. K. (2011). Overshooting of clean tropospheric air in the tropical lower stratosphere as seen by the CALIPSO lidar. *Atmospheric Chemistry and Physics*, *11*(18), 9683–9696. doi: 10.5194/acp-11-9683-2011

Virts, K. S., & Houze, R. A. (2015). Clouds and Water Vapor in the Tropical Tropopause Transition Layer over Mesoscale Convective Systems. *Journal of the Atmospheric Sciences*, *72*(12), 4739–4753. doi: 10.1175/JAS-D-15-0122.1

Wu, X., Fu, Q., & Kodama, C. (2023). Response of Tropical Overshooting Deep Convection to Global Warming Based on Global Cloud-Resolving Model Simulations. *Geophysical Research Letters*, *50*(14), e2023GL104210. doi: 10.1029/2023GL104210

Xian, T., & Fu, Y. (2015). Characteristics of tropopause-penetrating convection determined by TRMM and COSMIC GPS radio occultation measurements. *Journal of Geophysical Research: Atmospheres*, *120*(14), 7006–7024. doi: 10.1002/2014JD022633

Xie, F., Li, J., Tian, W., Li, Y., & Feng, J. (2015). Indo-Pacific Warm Pool Area Expansion, Modoki Activity and Tropical Cold-Point Tropopause Temperature Variations. *Scientific Reports*, *4*(1), 4552. doi: 10.1038/srep04552

Yang, G.-Y., & Slingo, J. (2001). The Diurnal Cycle in the Tropics. *MONTHLY WEATHER REVIEW*, *129*, 18.

Zhou, X., & Holton, J. R. (2002). Intraseasonal Variations of Tropical Cold-Point Tropopause Temperatures. *Journal of Climate*, *15*(12), 1460–1473. doi: 10.1175/1520-0442(2002)015⟨1460:IVOTCP⟩2.0.CO;2

Zhou, X.-L., Geller, M. A., & Zhang, M. (2001a). Cooling trend of the tropical cold point tropopause temperatures and its implications. *Journal of Geophysical Research: At-*

mospheres, *106*(D2), 1511–1522. doi: 10.1029/2000JD900472

Zhou, X. L., Geller, M. A., & Zhang, M. H. (2001b). Tropical Cold Point Tropopause Characteristics Derived from ECMWF Reanalyses and Soundings. *Journal of Climate*, *14*(8), 1823–1838. doi: 10.1175/1520-0442(2001)014⟨1823:TCPTCD⟩2.0.CO;2

Zipser, E. J., Cecil, D. J., Liu, C., Nesbitt, S. W., & Yorty, D. P. (2006). WHERE ARE THE MOST INTENSE THUNDERSTORMS ON EARTH? *Bulletin of the American Meteorological Society*, *87*(8), 1057–1072. doi: 10.1175/BAMS-87-8-1057

Zängl, G., Reinert, D., Rípodas, P., & Baldauf, M. (2015). The ICON (ICOsahedral Non-hydrostatic) modelling framework of DWD and MPI-M: Description of the non-hydrostatic dynamical core. *Quarterly Journal of the Royal Meteorological Society*, *141*(687), 563–579. doi: 10.1002/qj.2378